



**HAL**  
open science

## A New Conceptual Picture of the Trade Wind Transition Layer

Anna Lea Albright, Bjorn Stevens, Sandrine Bony, Raphaela Vogel

► **To cite this version:**

Anna Lea Albright, Bjorn Stevens, Sandrine Bony, Raphaela Vogel. A New Conceptual Picture of the Trade Wind Transition Layer. *Journal of the Atmospheric Sciences*, 2023, 80 (6), pp.1547-1563. 10.1175/JAS-D-22-0184.1 . hal-04310329

**HAL Id: hal-04310329**

**<https://hal.science/hal-04310329v1>**

Submitted on 25 Nov 2024

**HAL** is a multi-disciplinary open access archive for the deposit and dissemination of scientific research documents, whether they are published or not. The documents may come from teaching and research institutions in France or abroad, or from public or private research centers.

L'archive ouverte pluridisciplinaire **HAL**, est destinée au dépôt et à la diffusion de documents scientifiques de niveau recherche, publiés ou non, émanant des établissements d'enseignement et de recherche français ou étrangers, des laboratoires publics ou privés.



Distributed under a Creative Commons Attribution 4.0 International License

## A New Conceptual Picture of the Trade Wind Transition Layer

ANNA LEA ALBRIGHT<sup></sup><sup>a</sup>, BJORN STEVENS<sup></sup><sup>b</sup>, SANDRINE BONY<sup></sup><sup>a</sup>, AND RAPHAELA VOGEL<sup></sup><sup>a</sup>

<sup>a</sup> *Laboratoire de Météorologie Dynamique, CNRS, Sorbonne Université, Ecole Normale Supérieure, Ecole Polytechnique, Paris, France*

<sup>b</sup> *Max Planck Institute for Meteorology, Hamburg, Germany*

(Manuscript received 25 August 2022, in final form 27 February 2023, accepted 6 March 2023)

**ABSTRACT:** The transition layer in the trades has long been observed and simulated, but the physical processes producing its structure remain little investigated. Using extensive observations from the *Elucidating the Role of Clouds–Circulation Coupling in Climate* (EUREC<sup>4</sup>A) field campaign, we propose a new conceptual picture of the trade wind transition layer, occurring between the mixed-layer top (around 550 m) and subcloud-layer top (around 700 m). The theory of cloud-free convective boundary layers suggests a transition-layer structure with strong jumps at the mixed-layer top, yet such strong jumps are only observed rarely. Despite cloud-base cloud fraction measured as only  $5.3\% \pm 3.2\%$ , the canonical cloud-free convective boundary layer structure is infrequent and confined to large [ $O(200)$  km] cloud-free areas. We show that the majority of cloud bases form within the transition layer, instead of above it, and that the cloud-top height distribution is bimodal, with a first population of very shallow clouds (tops below 1.3 km) and a second population of deeper clouds (extending to 2–3 km depth). We then show that the life cycle of this first cloud population maintains the transition-layer structure. That is, very shallow clouds smooth vertical thermodynamic gradients in the transition layer by a condensation–evaporation mechanism, which is fully coupled to the mixed layer. Inferences from mixed-layer theory and mixing diagrams, moreover, suggest that the observed transition-layer structure does not affect the rate of entrainment mixing, but rather the properties of the air incorporated into the mixed layer, primarily to enhance its rate of moistening.

**SIGNIFICANCE STATEMENT:** The physical processes producing the structure of the trade wind transition layer, a thin atmospheric layer thought to be important for regulating convection, are not yet well understood. Using extensive observations from a recent field campaign, we find that the cloud-free convective boundary layer structure, with an abrupt discontinuity in thermodynamic variables, is infrequent, despite cloud-base cloud fraction being small. We show that very shallow clouds both forming and dissipating within the transition layer smooth vertical gradients compared to a jump, except in large [ $O(200)$  km] cloud-free areas. This condensation–evaporation mechanism, which is fully coupled to the mixed layer, does not appear to affect the rate of entrainment mixing, but rather the properties of air incorporated into the mixed layer.


**KEYWORDS:** Marine boundary layer; Cumulus clouds; Diabatic heating; Mixing; Stability; Buoyancy

### 1. Introduction

The transition layer in the trades is often associated with a thin layer (100–200 m thick) at the interface between the turbulent mixed layer (around 500–600 m depth in the trades) and the overlying cloud layer. It is typically identified from vertical moisture and temperature gradients that differ from the nearly zero vertical gradients in the mixed layer below and different vertical gradients in the cloud layer (e.g., Malkus 1958; Augstein et al. 1974; Betts 1976; Yin and Albrecht 2000). This layer has long been observed (e.g., Malkus 1958; Augstein et al. 1974;

Betts 1976; Yin and Albrecht 2000) and simulated (e.g., Stevens et al. 2001). The physical processes that give rise to its structure are, however, still not well understood.

There are numerous ambiguities related to the identification of the transition layer and its characteristics. One such ambiguity is whether the transition layer is a ubiquitous feature of the trade wind atmosphere in both cloud-topped versus cloud-free boundary layers, as well as within cloudy versus clear soundings taken in cloud-topped boundary layers. Malkus (1958), for instance, examines vertical gradients in 25 trade wind soundings to conclude that the transition layer was always (100%) present in clear-sky regions and generally (55%) absent in cloudy regions, but from this analysis it was difficult to ascertain whether the clear-sky soundings were taken in larger areas of clear skies, as might be associated with a cloud-free boundary layer, or in the clear-sky portions of cloud-topped boundary layers. Malkus also proposed that the transition layer is thicker in clear soundings (200 m) than in cloudy soundings (80 m), as illustrated schematically in Fig. 1a. Betts (1976) also highlights differences in the profiles of temperature and mixing ratio, as well as the lifting condensation level, for cloudy and clear-sky soundings.

 Denotes content that is immediately available upon publication as open access.

Vogel's current affiliation: Meteorological Institute, Center for Earth System Research and Sustainability, Universität Hamburg, Hamburg, Germany.

*Corresponding author:* Anna Lea Albright, anna-lea.albright@lmd.ipsl.fr

DOI: 10.1175/JAS-D-22-0184.1

© 2023 American Meteorological Society. For information regarding reuse of this content and general copyright information, consult the [AMS Copyright Policy](#) ([www.ametsoc.org/PUBSReuseLicenses](http://www.ametsoc.org/PUBSReuseLicenses)).

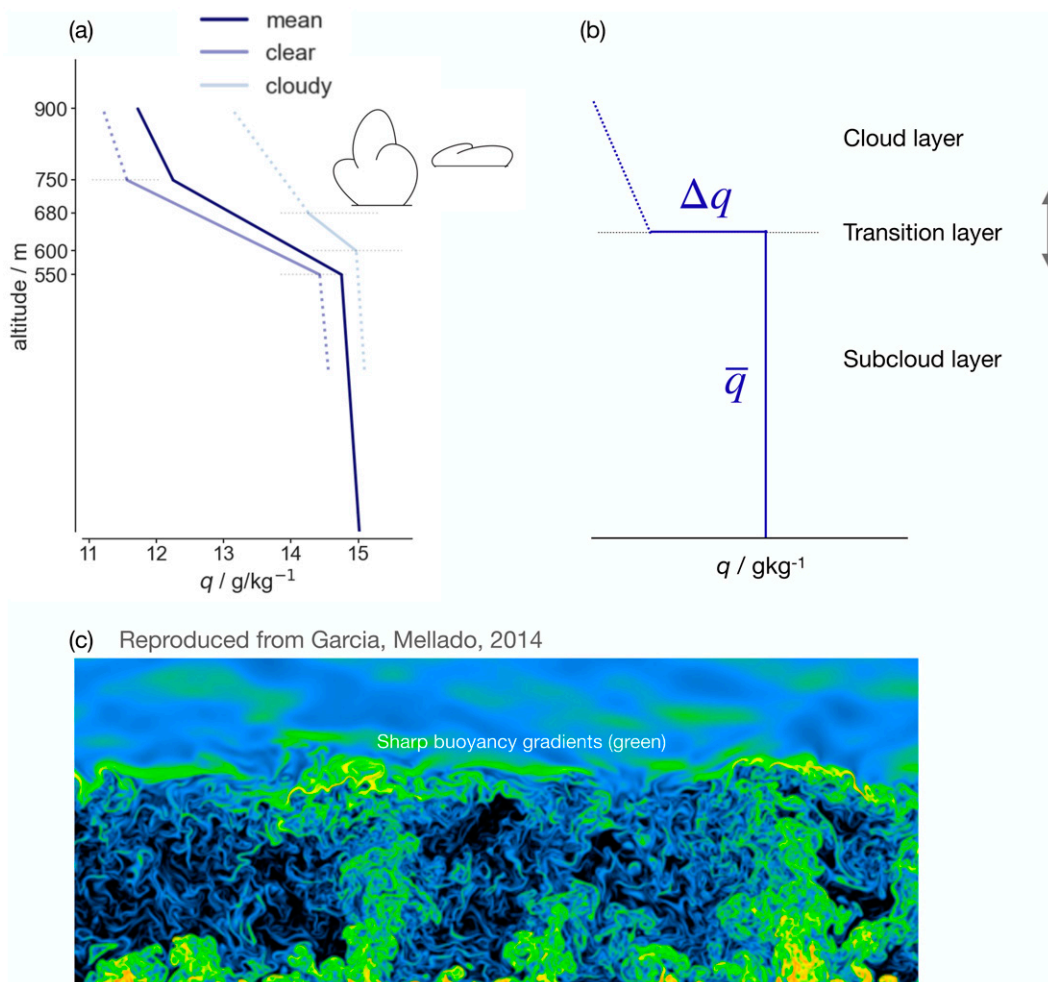


FIG. 1. (a) Representing specific humidity profiles from Malkus (1958) with the heights and gradients given in that study. The mean profile (dark blue) is the weighted average between 16 clear-sky (averaged in light blue) and 9 cloudy (averaged in medium blue) soundings. The transition-layer gradients are shown in solid lines in the clear and cloudy profiles compared to dashed lines for the mixed and cloud layers. According to this view, clouds start to form above the transition-layer top. (b) An idealized profile of specific humidity similar to those in previous conceptual models (e.g., Arakawa and Schubert 1974; Albrecht et al. 1979; Stevens 2006). That the infinitely thin transition layer can vary in height is indicated by the up-and-down arrow. (c) Figure reproduced from Garcia and Mellado (2014) (their Fig. 2), showing the logarithm of the buoyancy gradient (similar to the  $\theta_v$  gradient) from their direct numerical simulation of a dry convective boundary layer. Colors correspond to increasing values, from black to blue to green.

Another ambiguity relates to where cloud base is located relative to the transition layer. Early observational studies placed cloud base *above* the transition-layer top (Malkus 1958; Augstein et al. 1974). Augstein et al. (1974), for instance, proposes a qualitative scheme (their Fig. 12) that the trade wind transition layer is maintained by dry convection and mechanically driven turbulence, whereas clouds form and moist convective processes play a role in producing the vertical structure above the transition-layer top. More recent conceptual model studies contend that cloud bases form within the transition layer (Neggers et al. 2009; Gentine et al. 2013), yet their conceptualization of the transition layer remains somewhat ambiguous: in Neggers et al. (2009), the mixed-layer top and cloud base coincide, but what they call the transition

layer is above these two levels; Gentine et al. (2013) call the offset between the mixed layer and cloud layer the “dry inversion layer,” with cloud bases occurring somewhere within this layer. Inferences of strong vertical potential temperature gradients over the transition layer and cloud bases forming above the transition-layer top established a conceptual picture of the transition layer as a barrier to convection that regulates subcloud- to cloud-layer transports (e.g., Ooyama 1971; Augstein et al. 1974; Yin and Albrecht 2000; Neggers et al. 2006).

In the years subsequent to these early observational studies, modeling studies idealized the trade wind transition layer as an infinitely thin layer exhibiting a “jump,” or abrupt discontinuity, above the well-mixed layer. This idealization—clearly recognized as a simplification of reality—was made in analogy

with stratocumulus regimes (e.g., Lilly 1968) or cloud-free convective boundary layer (e.g., Stull 1976; Tennekes 1973; Arakawa and Schubert 1974; Albrecht et al. 1979; Stevens 2006). Such a conceptual view is shown in Fig. 1b. A cloud-free direct numerical simulation exhibiting a strong vertical gradient at the mixed-layer top is reproduced in Fig. 1c (Garcia and Mellado 2014). These illustrations highlight a mixed layer that is well mixed by turbulence, and capped locally by an abrupt discontinuity. To the extent a transition layer or entrainment zone emerges, it is associated with deformation between updraft plumes, or with the statistical signature of undulations in the capping layer, so that it is not generally thought of as a mixing layer. In the trades, the maximum cloud-base cloud fraction is small. It was recently measured to be  $5.3\% \pm 3.2\%$  [mean and standard deviation from 20 flights from a lidar-radar synergy product in Bony et al. (2022)]. Given this small cloud-base cloud fraction, it appears reasonable to assume that the transition-layer structure with strong jumps is the baseline structure, as in Stevens (2006).

As part of the *Elucidating the Role of Clouds–Circulation Coupling in Climate* (EUREC<sup>4</sup>A) field campaign, which took place east of Barbados in January and February 2020 (Bony et al. 2017; Stevens et al. 2021), we collected the necessary data to investigate the structure of the trade wind transition layer and the physical processes that produce this structure. In a previous paper (Albright et al. 2022) it was shown that a transition layer can be identified on the basis of vertical thermodynamic profiles. That same analysis highlighted how the presence of a finitely thick transition layer introduced ambiguity into the application of mixed-layer theory to the quantification of subcloud-layer moisture and heat budgets.

The ambiguity arises because in the presence of a transition layer, jumps are not well defined. To estimate the entrainment velocity (Albright et al. 2022) adopted an effective mixing layer of depth  $h$  which they associated with the subcloud layer, and related the entrainment velocity  $V_1$  to effective jumps such that

$$V_1 C_1 [\overline{\theta_v}(h + \delta h) - \overline{\theta_v}] = -\overline{w'\theta_v}|_1 = A_e \overline{w'\theta_v}|_0. \quad (1)$$

In this expression,  $\theta_v$  denotes the virtual potential temperature, overlines denote means over the mixing layer, and the “jumps” are implicitly defined as some fraction of the difference between the mixed-layer values, and some value well ( $\delta h$ ) above the mixing layer, which introduces the parameter  $C_1$ ;  $A_e$  then determines the effective buoyancy flux that would be required at the top of a mixed layer to balance the mixed-layer budgets. A Bayesian framework was then used to estimate the free parameters,  $C_1$  and  $A_e$ , where  $C_1$  was allowed to vary between the moisture and heat budgets but converged to similar values. This resulted in a value of  $A_e = 0.43$ , which was substantially larger than its canonical value of 0.2, raising the question as to why, and whether the physical processes that give rise to the structure of the trade wind transition layer could be identified in ways that might explain this apparent discrepancy.

In section 2, we introduce the data used in this study. We then briefly review the method to define the transition layer from thermodynamic profiles from Albright et al. (2022)

(section 3a) and compare our conceptual view with past studies (sections 3b and 3c). In section 4, we discuss the physical mechanisms producing the observed transition-layer structure. Finally, section 5 explores impacts of the transition-layer structure on entrainment mixing efficiency, mixed-layer thermodynamic state, and surface fluxes, before presenting discussion and conclusions in section 6.

## 2. EUREC<sup>4</sup>A field campaign data and large-eddy simulation output

We primarily use observations from the EUREC<sup>4</sup>A field campaign. First, we employ 810 dropsondes from the High Altitude and Long Range Research Aircraft (HALO) operated between 22 January and 15 February 2020 (Konow et al. 2021). These dropsondes provide vertical profiles of pressure, temperature, relative humidity, and wind, which have been processed and interpolated into a common altitude grid with 10 m vertical resolution (George et al. 2021). As described in Albright et al. (2022), dropsonde measurements were distributed along the “EUREC<sup>4</sup>A circle,” defined by a circular flight pattern with an approximately 220 km diameter, centered at 13.3°N, 57.7°W. The spatial scale of the EUREC<sup>4</sup>A circle corresponds to the “meso- $\beta$ ,” or mesoscale environment on scales 20–200 km as defined by Orlanski (1975), or the typical size of a climate model grid box. A “circle mean” averages about 12 dropsondes along the EUREC<sup>4</sup>A circle over the course of about 1 h. A “circling mean” is the average of three such circle means, and thus each circling mean comprises about 36 dropsondes over about 3 h. Typically, each flight incorporated two—temporally well-separated—periods of circling. This circular flight pattern was repeated 69 times, yielding 69 one-hour circle means and 24 three-hour circling means, over 12 flights. Given that measurements did not target specific meteorological conditions they provide unbiased statistical sampling of the environment. On the EUREC<sup>4</sup>A circle-mean scale, George et al. (2021) also calculate divergence and vertical velocity from horizontal wind measurements following Bony and Stevens (2019), and we employ these circle-mean vertical velocity measurements in the present study. Also used are clear-sky, aerosol-free radiative heating profiles from Albright et al. (2021).

To estimate cloud-base heights, we use ceilometer cloud-base height estimates from two platforms, the R/V *Meteor* and the Barbados Cloud Observatory (BCO; Stevens et al. 2016), at 10-s resolution from 19 January to 19 February 2020. The R/V *Meteor* sailed within the eastern portion of the EUREC<sup>4</sup>A circle, whereas the BCO is about 200 km downstream from the circle center. Data during nighttime that the HALO aircraft did not fly are dropped. Cloud-base heights vary, and to estimate the base of clouds forming from updrafts within the subcloud layer, the first-detected cloud-base heights [as in Nuijens et al. (2014): “cbh<sub>1</sub>, where the superscript 1 denotes it is the first detected base, rather than the second or third”] between 350 and 1000 m are analyzed. We bin data into 3-hourly segments and then select the most frequently sampled value as a representative cloud base. Typically, the first peak corresponds to the absolute peak of the

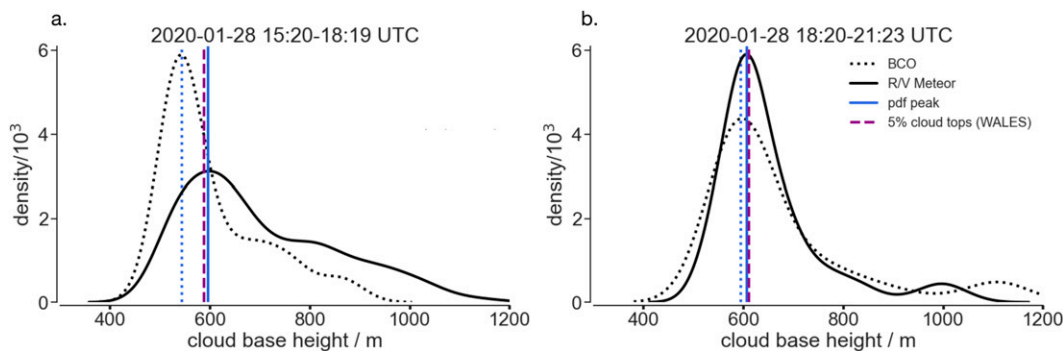


FIG. 2. Example 3-hourly cloud-base height distributions from the R/V *Meteor* ceilometer (black solid) and the Barbados Cloud Observatory (BCO) ceilometer (black dotted), annotated with the first distribution peak (“pdf peak,” blue vertical line, either solid for the R/V *Meteor* or dotted for the BCO). Also shown is the 5% quantile of the cloud-top height distribution estimated from WALEs lidar for the same time interval (purple dashed vertical line). The unit “density/10<sup>3</sup>” is chosen so the axis labels round to single digits.

distribution. In the cases where they differ, we select the first peak that is within 50% of the absolute distribution peak. The first peak is chosen because the first decile is biased by rain, whereas higher deciles increasingly reflect cloud side detection from sheared convection or decaying cloud fragments that are not indicative of cloud base (Nuijens et al. 2014). Two examples of 3-hourly cloud-base distributions are given in Fig. 2 to illustrate the methodology. In the following analysis, the ceilometer cloud-base height distribution refers to the aggregate of distribution peaks from 3-hourly data (e.g., in Fig. 3c).

Cloud-top height data are taken from the *Water vapor Lidar Experiment in Space* (WALEs) instrument, a water vapor differential absorption lidar. This lidar operates at four wavelengths around 935 nm to measure water vapor mixing ratio profiles below the HALO aircraft (Wirth et al. 2009; Konow et al. 2021). Data products used are a cloud flag and cloud-top height having both a precision and accuracy of about 10 m (Konow et al. 2021). By way of comparison, even high-resolution satellite retrievals from the Advanced Spaceborne Thermal Emission and Reflection Radiometer instrument have a vertical uncertainty of 250–500 m on cloud-top height estimates (e.g., Mieslinger et al. 2019), rendering the WALEs cloud-top height estimates with their high vertical resolution particularly valuable.

For the purposes of comparison, we also use output from a large-eddy simulation (LES) of the tropical Atlantic, east of Barbados, to be comparable with the EUREC<sup>4</sup>A campaign (Dauhut et al. 2023). This simulation is on a 100 km × 200 km grid, with 100 m horizontal and 40 m vertical grid spacing and time step of one second over a 7 h simulation. The simulation focused on a case study of 2 February 2020 that resolved an about 100 km diameter cluster of clouds known as a “flower cloud” (e.g., Stevens et al. 2020; Bony et al. 2020).

### 3. Identifying the transition layer using EUREC<sup>4</sup>A observations

In this section, we first summarize a method to identify the transition-layer location and depth from observed thermodynamic

profiles (section 3a). We then discuss the stability of this layer in terms of potential temperature gradients (section 3b) and where the transition layer is located relative to cloud-base heights (section 3c).

#### a. Defining the transition-layer depth

A method for identifying the transition-layer location and its depth from vertical thermodynamic profiles is given in Albright et al. (2022) and summarized here. The transition layer is known to occur above the mixed-layer top, but definitions demarcating these layers are often imprecise, if not conflicting (e.g., Malkus 1958; Augstein et al. 1974; Betts 1976; Yin and Albrecht 2000). One general approach, which we call the jump or gradient method, is to identify the mixed-layer top as the height at which a given profile deviates from being well mixed vertically, by a certain threshold (e.g., Canut et al. 2012). We apply this method to different thermodynamic variables, including specific humidity  $q$ , potential temperature  $\theta$ , and virtual potential temperature  $\theta_v = \theta(1 + 0.608q)$ . A closely related method is to identify the mixed-layer top with the height where the relative humidity maximizes. Another, somewhat different method, which we call the parcel method, identifies a mixing (rather than a mixed) layer with the level of neutral buoyancy, measured by  $\theta_v$ , of a surface parcel.

Applying the jump method to  $q$ ,  $\theta$ , and  $\theta_v$ , we find a bimodal distribution, with a first layer corresponding to a well-mixed layer in  $q$  and  $\theta$ —which also corresponds to the distribution of relative humidity maxima—and a second layer that is well mixed in  $\theta_v$  and corresponds to the parcel method height distribution. We find such a bimodal distribution across all scales of aggregation, from individual dropsondes (Fig. 3a) to 1-h circle-mean and 3-h circling-mean data. This consistency across scales indicates that the height bimodality is not simply a function of aggregating soundings. The first height distribution has a mean depth of 500 m for individual soundings and 555 m for circle-mean data (Figs. 3a,b). This mean height is found by averaging the  $q$  jump,  $\theta$  jump, and relative humidity maxima distribution. A layer that is well mixed vertically in  $q$  and  $\theta$  has previously been called the mixed layer (e.g., Malkus 1958;



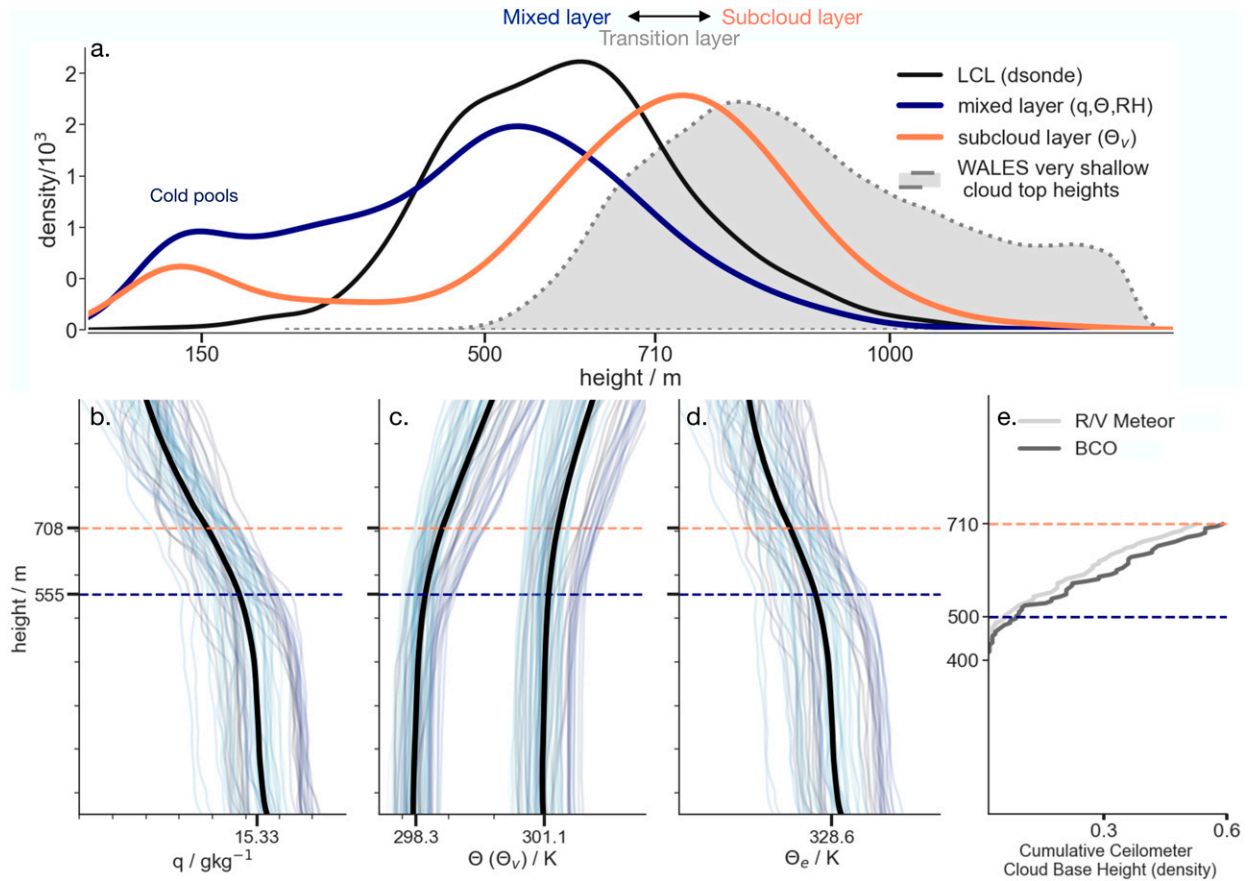


FIG. 3. Methodology of defining the transition layer. Figure adapted from Albright et al. (2022) but related to cloud-base and cloud-top heights. (a) Distributions of different height methods, as described in section 3a, applied to 810 dropsondes to estimate the mixed- and subcloud-layer heights. Height distributions are shown for the mixed layer (blue, averaging three methods based on  $q$  and  $\theta$  individually, and relative humidity), subcloud layer (orange, averaging the  $\theta_v$ -gradient and parcel method), and the lifting condensation levels calculated from individual dropsonde soundings (black). Also shown is the distribution of cloud-top heights of very shallow clouds below 1.3 km estimated from the WALES lidar (gray filled distribution). (bottom) Sixty-nine circle-mean profiles for (b)  $q$ , (c)  $\theta$  and  $\theta_v$ , and (d)  $\theta_e$ , across time (from darker to lighter blue), as well as their time mean (black). Dotted lines mark the mixed-layer height (blue) and subcloud-layer height (orange) calculated using circle-mean data. Note that the mixed-layer and subcloud-layer height values in (b) are calculated from circle-mean profiles, explaining the difference in heights with (a) calculated from individual soundings. (e) The empirical cumulative distribution function of aggregated ceilometer cloud-base height distributions measured by the R/V Meteor (light gray) and at the BCO (darker gray), as described in section 2.

Augstein et al. 1974), and we adopt this same terminology. The lower mean mixed-layer-top height averaged across individual soundings is likely due to the presence of cold pool soundings (Touzé-Peiffer et al. 2022), which are well mixed to a much lower altitude, around 150 m (see Fig. 3a).

The buoyancy variable,  $\theta_v$ , by contrast, remains better mixed over a deeper layer. Such a layer that is better mixed deeper in  $\theta_v$  than  $q$  and  $\theta$  individually was observed previously and referred to as the subcloud layer, often corresponds to the environmental-mean lifting condensation levels (e.g., Malkus 1958; Augstein et al. 1974; Nicholls and Lemone 1980; Yin and Albrecht 2000). In our observations, the subcloud-layer top has a mean depth of 710 m in individual soundings and 708 m in circle-mean data. We continue to call this the “subcloud” layer, although the nomenclature can be confusing because clouds already start to form below the top of this

layer. Indeed, calculating the lifting condensation levels from individual soundings—rather than circle-mean or circling-mean data that represent environmental-mean air—shows that the moistest profiles already have their lifting condensation levels closer to the mixed-layer top, with values  $604 \pm 152$  m denoting the mean and standard deviation (Fig. 3a).

This bimodal distribution stands in contrast with the conceptual idealization of a well-mixed layer topped by an abrupt discontinuity, or an infinitely thin transition layer. We associate this ambiguous vertical region—the difference between the subcloud-layer-top and mixed-layer-top distributions—with the transition layer. That is, we define the transition layer as the difference between the subcloud-layer top and mixed-layer top, in both individual soundings and aggregated profiles. Using individual dropsondes and taking the difference between the top of the subcloud-layer and mixed-layer distributions, we find a

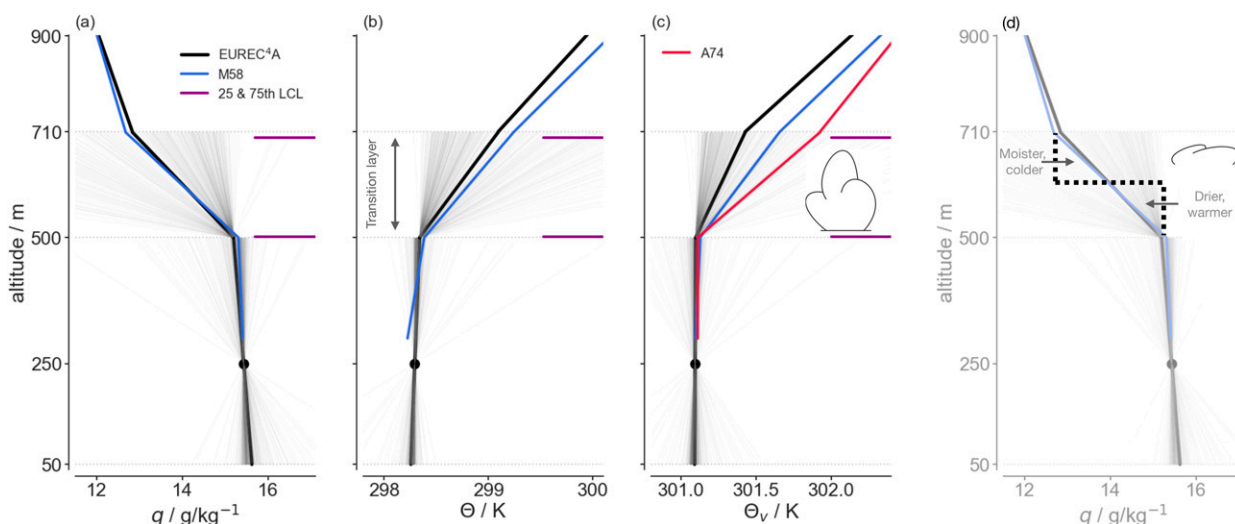


FIG. 4. Composite profiles of (a) specific humidity  $q$  and (b) virtual potential temperature  $\theta_v$ . EUREC<sup>4</sup>A data are plotted in black, both the campaign mean (thick black line) and individual dropsondes (thin gray lines), with the mixed-layer mean value indicated by the black dot (disregard the dot's height; it is simply half the mixed-layer height). M58 (blue) corresponds to Malkus (1958), and A74 (red) refers to Augstein et al. (1974).  $\theta_v$  gradients are given in Augstein et al. (1974), with mean values adjusted to the mean mixed-layer value in EUREC<sup>4</sup>A for purposes of comparison. For Malkus (1958),  $\theta_v$  values are calculated from observed temperature, mixing ratio, and pressure profiles in her Fig. 7. Note, moreover, that the visualization in Fig. 4 exaggerates the extent of the strongest vertical gradients by extrapolating these strong vertical gradients, which are often found over short distance, over the mean depth of the transition layer. Also shown are the 25th and 75th percentiles of lifting condensation levels (LCL; purple solid line) calculated from individual dropsondes, wherein each LCL value per sonde is the mean of the distribution of LCL values calculated every 10 m from 100 to 300 m. (d) The conceptual picture [on top of the  $q$  profile from (a), albeit with increased transparency] by which the condensation–evaporation dipole leads to smoother gradients, compared to a jump (idealized dotted black line), by first drying and warming, and then moistening and cooling.

transition-layer thickness of  $180 \pm 207$  m, with the values denoting the mean and standard deviation. The values are  $151 \pm 77$  m for circle-mean and  $152 \pm 50$  m for circling-mean data, converging toward a mean depth of about 150 m and smaller standard deviation for increasing scales of averaging. That the difference is larger for individual soundings again likely relates to the presence of cold pool soundings, which have very shallow mixed layers (see Fig. 3a). The estimated transition-layer depth is consistent with previous observational ranges between 100 and 200 m depth (e.g., Malkus 1958; Augstein et al. 1974; Yin and Albrecht 2000).

### b. Transition-layer stability

Some previous conceptualizations of the transition layer contend that the transition layer acts as a barrier or cap to convection (section 1), which would suggest relatively strong thermodynamic gradients. The transition-layer gradients given in Malkus (1958) and Augstein et al. (1974) are a useful point of comparison. Figure 4 shows that transition-layer  $\theta$  and  $\theta_v$  gradients observed during EUREC<sup>4</sup>A (black line) are, on average, weaker than those in Malkus (1958) and Augstein et al. (1974). Specific humidity gradients are similar, and the weaker  $\theta_v$  gradient in EUREC<sup>4</sup>A is driven by a slightly weaker mean  $\theta$  gradient. These composite profiles are constructed from the mean mixed-layer value; mean gradients over the mixed layer, transition layer, and cloud layer (from 710 to 1800 m); and mean heights of the mixed layer and transition-layer top calculated from individual soundings.

We speculate that the reason for the greater stability implied by the mean profiles in Malkus (1958) and Augstein et al. (1974) is their smaller sample size and that their sampling was not entirely unbiased, compared to the extensive, unbiased sampling in EUREC<sup>4</sup>A. Malkus (1958), for instance, launch 16 out of their 25 soundings in clear skies, whereas the other nine soundings explicitly targeted active cloud cores. The extent to which their clear sky soundings sampled cloud-free boundary layers, versus the clear-sky regions of cloud-topped boundary layers was difficult to ascertain. Augstein et al. (1974) analyze a larger set of soundings from field campaigns in 1965 and 1969. Soundings are, however, removed when a transition layer was not apparent, which could bias results toward stronger transition-layer gradients. During EUREC<sup>4</sup>A, strong gradients with the magnitude of those in Malkus (1958) and Augstein et al. (1974) are seen, but they occur infrequently (Fig. 4). That the transition layer is not always a more stable region than the cloud layer is more consistent with Betts (1976), who noted the absence of a marked stable layer near cloud base in averaged profiles. These figures also reinforce that the transition layer can be identified from vertical thermodynamic gradients that differ from those in the overlying cloud layer—in particular, a more negative  $q$  gradient and a less positive  $\theta_v$  gradient in the transition layer than in the cloud layer.

### c. Cloud bases form within the transition layer

Another difference with Malkus (1958) and Augstein et al. (1974) is that we find that the majority of cloud bases are

already found *within* the transition layer, instead of above its top. Examining ceilometer cloud-base estimates, about 60% of 3-h cloud-base peaks occur below the subcloud-layer-top height. A cumulative distribution of these cloud-base heights is given in Fig. 3e, showing that the R/V *Meteor* ceilometer has 61% of cloud-base peaks below 710 m (55% for the BCO ceilometer). Below 500 m, approximately the mixed-layer-top height, 6% of clouds measured by the R/V *Meteor* ceilometer already have their bases (9% clouds at BCO ceilometer). Clouds with bases below 500 m are likely associated with precipitation and not encompassed by the processes considered in the present manuscript, though we still include this small fraction of clouds in the analysis.

Cloud bases therefore form close to the mixed-layer top (Fig. 3a), with the majority of cloud bases having formed at the subcloud-layer top (Fig. 3e). In Vogel et al. (2022), the subcloud-layer top corresponds to what is measured as the maximum level of cloud-base cloudiness. Another way of conceptualizing the transition-layer depth—not from thermodynamic profiles but rather based on cloudiness—is thus that the transition layer spans the level from cloud base to the level of maximum cloud-base cloudiness.

Given that the majority of clouds already have their bases within the transition layer, we conjecture that cloud-mediated processes could play a role in creating its structure. Many clouds may continue to grow above the transition layer, yet a substantial fraction of clouds both form and dissipate within the transition layer. When clouds form, they warm and dry the ambient environment, and when they dissipate, they cool and moisten the environment, such that this air takes on properties that more closely resemble mixed-layer air. Such cloud-driven processes could “precondition” the surrounding air and reduce the work to entrain more-buoyant air into the mixed layer. We thus hypothesize that 1) the structure of the transition layer is an important way in which the cloud-topped boundary layer (CTBL) differs from a cloud-free, or dry boundary layer (CFBL), and 2) these different vertical structures could influence entrainment mixing and the state of the mixed layer. These hypotheses can directly be tested using EUREC<sup>4</sup>A observations.

#### 4. Physical origins of transition-layer structure

##### a. Does the presence of clouds change the transition-layer structure?

We first test the idea that the presence of clouds changes the transition-layer structure through a denial-of-mechanism approach. As before we distinguish a CFBL from a CTBL, whereby in the latter, cumulus clouds, even very small cumulus clouds, top updrafts rising through the mixed layer. Because the CTBLs that we sample tend to have a small cumulus cloud fraction, most soundings we analyze are of clear skies. We distinguish large cloud-free regions (>100 km<sup>2</sup> area devoid of clouds) from clear-sky areas between the clouds, because the area between clouds within the CTBL will still be influenced by cloud condensate detrainment and mixing from previous, “ghost”

clouds. We identify CFBLs: first, by eye, from GOES-E satellite movies at 1-min resolution overlain with dropsonde locations and times (Bony et al. 2022); and second, using the cloud flag product from WALES lidar to select large cloud-free areas, as described in section 4b.

Figure 5 illustrates two case studies, for 22 January (Figs. 5a–e) and 2 February (Figs. 5f–j), both of which exhibit large clear-sky swaths. In each case, GOES-E satellite movies are used to identify one dropsonde from an extensive CFBL, spanning the diameter of the EUREC<sup>4</sup>A circle, and another sonde within a CTBL. The CFBL sondes exhibit a well-mixed-layer structure topped by a jump. In the CTBL sondes, a discontinuity is not visible, and instead there are smoother vertical gradients (Fig. 5). Examining the associated clear-sky radiative heating profiles (Albright et al. 2021) shows that CFBL profiles have peaks in radiative cooling associated with these sharper humidity gradients, whereas the CTBL profiles do not show any strong peak in radiative cooling (though such a cooling peak would be expected had we sampled clouds and accounted for condensate in the input to the radiative transfer calculations). The radiative heating peak at the top of the mixed layer, below the radiative cooling peak, is partly due to stronger shortwave solar absorption from water vapor in the cloud-free profile (not shown). Whether this radiative cooling–heating dipole sharpens the transition-layer humidity gradient or weakens it by engendering radiatively driven turbulence is a question that remains to be investigated.

To next test whether the expected difference between cloud-free (CFBL) and cloud-topped (CTBL) boundary layer profiles generalizes across the 810 dropsondes, we find the distribution of the maximum vertical gradient (over 10 m) in each dropsonde vertical profile of specific humidity,  $q$ , between 300 and 800 m. This maximum vertical gradient metric captures the strongest jump that is evident in an observed boundary layer moisture profile. The lower bound of 300 m is chosen to avoid possible surface-layer influences, and 800 m acts as a conservative estimate of the mixed-layer top. Results are similar for different choices of lower and upper bound, as well as for calculating more sustained vertical gradients (e.g., over 20, 50, or 100 m instead of 10 m). The vertical layering of the atmosphere is present in numerous variables, but particularly evident in moisture (e.g., Augstein et al. 1974), motivating our choice of  $q$ , though results are similar for other thermodynamic variables.

Figure 6 shows that the majority of soundings have small values of this maximum vertical gradient metric, corresponding to smooth gradients at the mixed-layer top. The 25th-percentile and median values of the maximum vertical gradient are 0.17 and 0.25 g kg<sup>-1</sup> compared to a standard deviation of 1.06 g kg<sup>-1</sup> for  $q$  averaged from 100 to 500 m. Examining vertical gradients above the 95th percentile compared to satellite images, we find that larger values systematically occur in large clear-sky areas. Figures 6b and 6c show satellite images for two days having numerous soundings making up the largest-5% vertical gradient values. On these days, large clear-sky areas frequently extend across the EUREC<sup>4</sup>A circle. This analysis provides an initial indication of an association



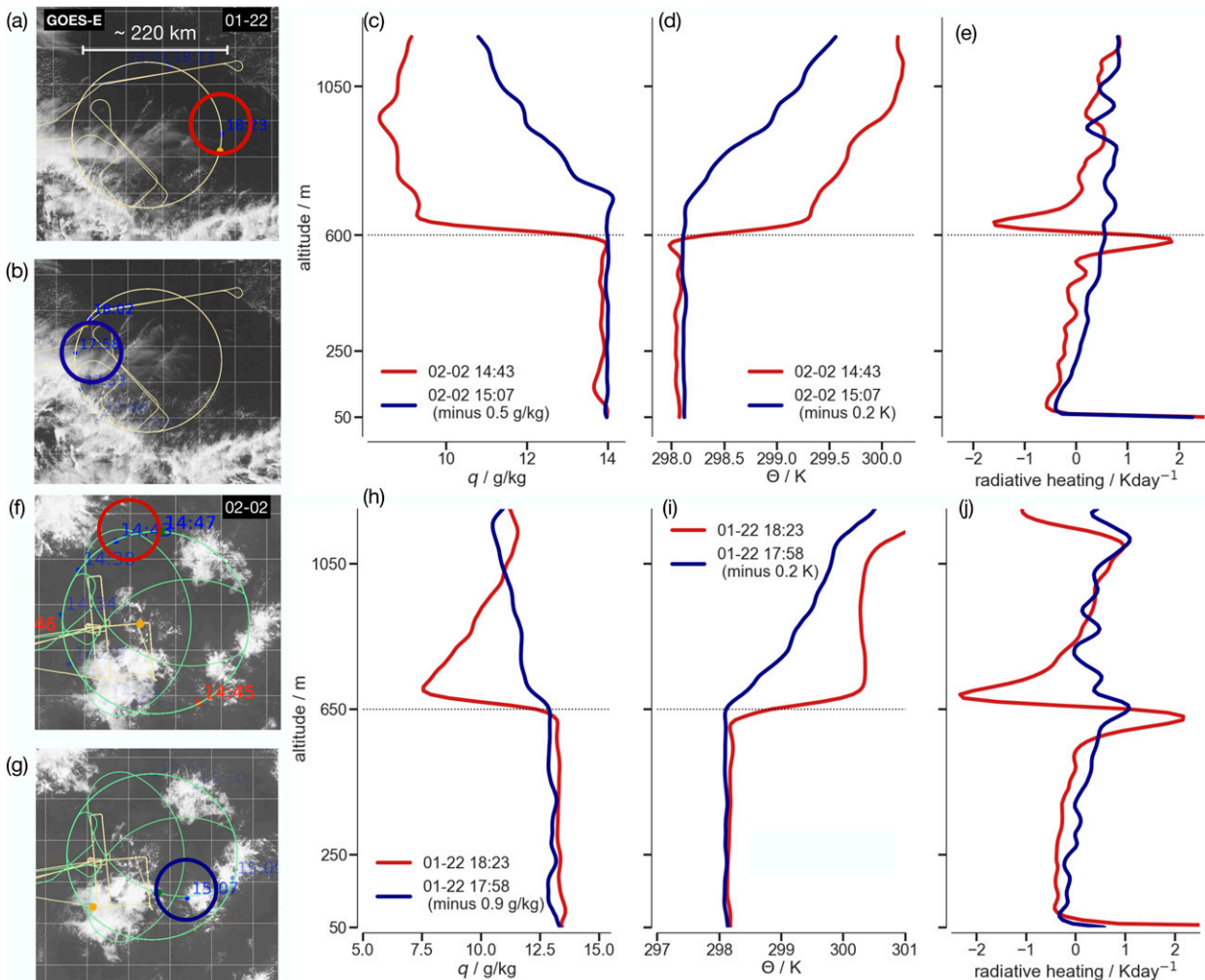


FIG. 5. Two pairs of dropsonde profiles for specific humidity  $q$ , potential temperature  $\theta$ , and net clear-sky, aerosol-free radiative heating profiles, wherein one sounding per pair is launched in a large clear-sky area (red) and the other in an area influenced by clouds (blue). Pairs of dropsondes are from (top) 22 Jan and (bottom) 2 Feb. (a),(b),(f),(g) Their corresponding GOES-E satellite images, which show mesoscale cloud organization patterns corresponding to (a),(b) “fish” and (f),(g) “flower” patterns (e.g., Stevens et al. 2020). The sonde times are given in the legends for dropsonde profiles, and the sonde location (outlined in blue or red circle) is overlain on the satellite image. Note that the vertical profiles are aligned to have approximately the same mixed-layer mean value to better compare the transition-layer structure; offsets are given in the legend.

between sharp gradients in thermodynamic profiles and large, cloud-free areas.

### b. Two populations of clouds

A population of clouds is identified that we hypothesize is responsible for changing vertical gradients in the transition layer of the CTBL relative to what is found in the CFBL. Figure 7 shows the distribution of cloud-top heights estimated from the WALES lidar (section 2; cf. Jacob et al. 2020). This cloud-top height distribution is bimodal, with peaks around 850 and 1900 m. The bimodality in cloud-top heights was previously identified (e.g., Genkova et al. 2007; Leahy et al. 2012), but the uncertainty on these early observational estimates (250–500 m) was large compared to the depth of the first cloud population and offset between shallow and deeper

clouds, and much larger than the uncertainty in the WALES cloud-top height data. There is an apparent scale separation around 1500 m, similar to the value of 1300 m used to separate two cloud populations simulated at the Barbados Cloud Observatory by large-eddy simulations in Vial et al. (2019). The first peak is associated with very shallow, likely nonprecipitating clouds, and the second peak is associated with deeper, potentially precipitating shallow clouds (Lonitz et al. 2015) and stratiform clouds resulting from detrainment near the trade wind inversion around 2–3 km. Very shallow clouds are more frequent than deeper clouds, and they appear to vary relatively little in height, with a standard deviation of 184 m for cloud tops below 1300 m (Fig. 7). A portion of these very shallow clouds has their tops within the transition layer, as can be seen in Fig. 3a.

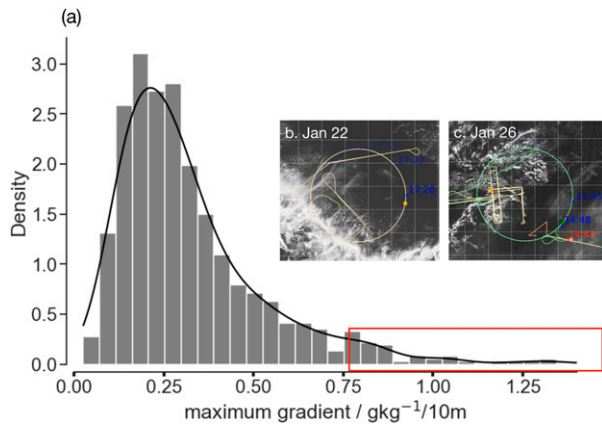


FIG. 6. (a) Distribution of the maximum vertical gradient (across 10 m) found in a given specific humidity  $q$  profile between 300 and 800 m. The red box highlights the largest-5% vertical gradients. (b),(c) Two example GOES-E satellite images illustrating large clear-sky swaths from which profiles with the largest-5% vertical gradients are drawn.

*c. Very shallow clouds appear to produce transition-layer structure*

To test how very shallow clouds influence the transition-layer structure, we revisit the maximum vertical gradient distribution (Fig. 6), but condition on scenes using cloud-top height estimates. The goal is to isolate large clear-sky swaths that are relatively free from cloud influences and compare the transition-layer structure in these cloud-free cases (which we associate with the CFBL) versus other cases (which we associate with the CTBL). Using the WALES cloud flag and cloud-top heights, measurements are separated into three categories: large clear-sky areas, cloudy areas with cloud tops below 1.3 km (shallow clouds; e.g., Fig. 7), and all areas that are not large clear-sky areas, including cloudy and smaller cloud-free areas (overlapping with the second category). This separation allows us to test whether 1) large clear-sky areas do systematically exhibit stronger vertical gradients in the transition layer, and 2) the presence of shallow clouds is sufficient to change the transition-layer structure from that found in the CFBL, independent of the influence of deeper clouds.

Large cloud-free areas are selected by first identifying all cloud-free segments using the cloud flag, calculating the 95th percentile of segment lengths, and then considering segments that are greater than this 95th percentile as large clear-sky areas. These large cloud-free patches are identified with the CFBL as they correspond to 15 min of flight time without encountering a cloud, or about 180 km at a typical flight speed of  $200 \text{ m s}^{-1}$ . The associated dropsondes are then selected for these large clear-sky areas, corresponding to 13% of all dropsondes. For cloudy areas, the disjoint set of the large clear-sky swaths is chosen, including clear-sky in between clouds, shallow clouds, and deeper clouds. The category of shallow clouds is selected by removing cases with cloud tops greater than 1.3 km.

We then repeat the analysis from Fig. 6 for these three categories. Figure 8 shows that the maximum vertical gradients

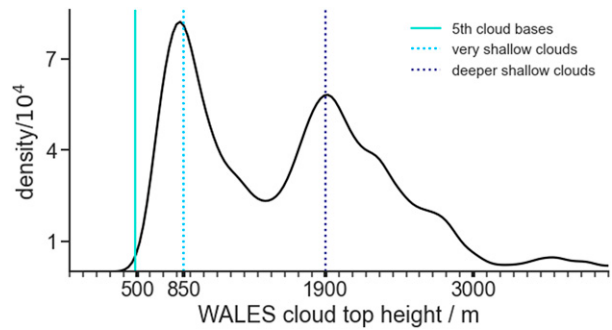


FIG. 7. Distribution of cloud-top heights estimated from WALES lidar data as described in section 2. Vertical dashed lines correspond to approximately the peaks in the bimodal distribution, around 850 m for shallower and 1900 m for deeper clouds. The solid turquoise line marks the 5th percentile of cloud-base heights estimated from R/V *Meteor* and BCO ceilometers, giving a lower bound of cloud-base heights. The unit “density/10<sup>4</sup>” is chosen so the axis labels round to single digits.

are indeed stronger in large clear-sky areas than other scenes. The distribution of gradients estimated for shallow clouds is, moreover, nearly identical with the distribution of gradients for all conditions (including deeper clouds).

To identify whether such associations might be causal we look for a statistical relationship between the maximum vertical gradients and a variety of environmental variables that might explain their strength, including surface wind speed, mixed-layer humidity and potential temperature, vertical velocity at various altitudes, cloud fraction at the level of its cloud-base maximum (measured from the ATR-42 aircraft, section 2), and the fraction of shallow clouds ( $<1.3 \text{ km}$ ) versus deeper clouds at cloud-base maximum cloudiness. We take the maximum vertical gradient (over 10 m) for the 810 dropsondes (as described in section 4a) and aggregate these values into circle-mean values. We then compare the circle-mean values to the mean mixed-layer state, the magnitude of the subsidence at different heights, and different measures of

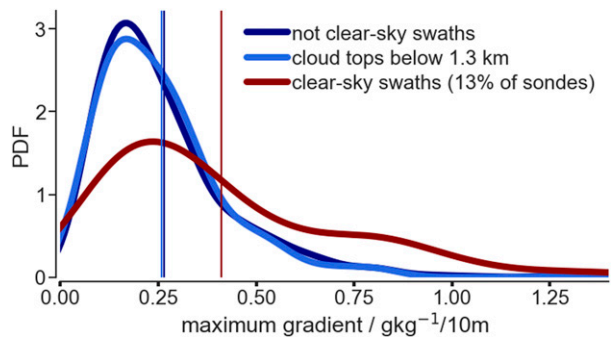


FIG. 8. As in Fig. 6, but with distributions conditioned on large clear-sky scenes of at least 15 min without encountering a cloud (red), shallow clouds with cloud-top heights estimated from WALES lidar data below 1.3 km (light blue), and all areas outside of large clear-sky scenes (dark blue). Each colored vertical line is the mean of the distributions.

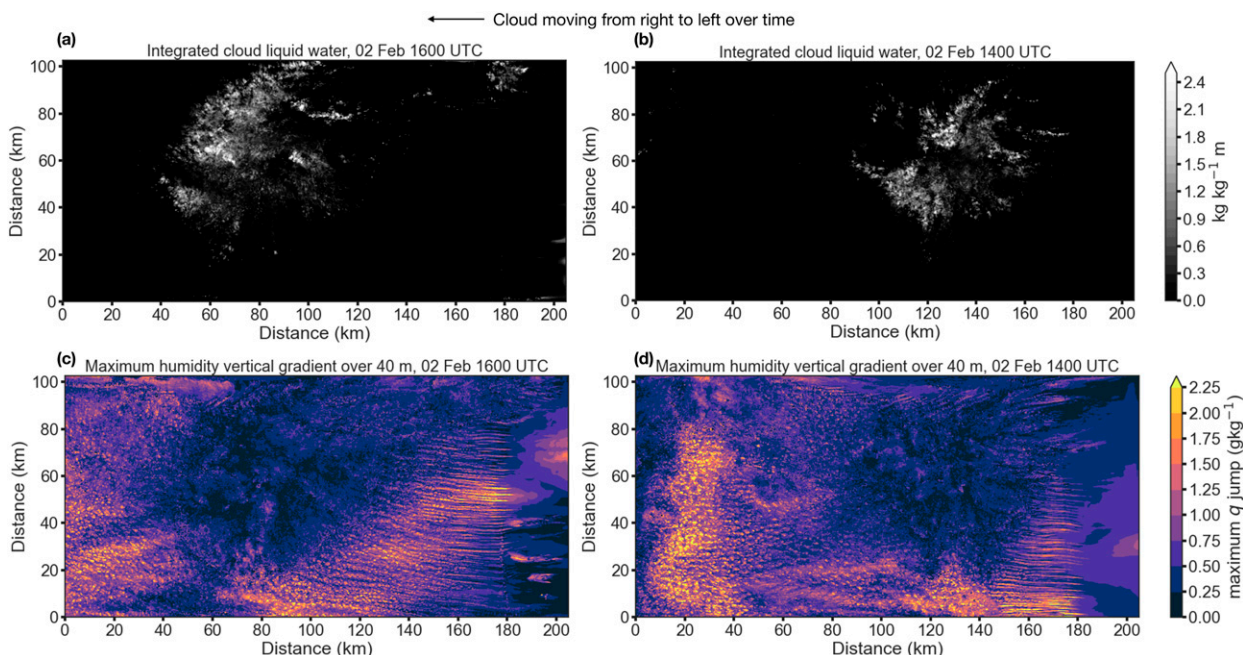


FIG. 9. Vertically integrated cloud liquid water content (in  $\text{kg kg}^{-1} \text{m}$ ) and the maximum vertical gradient in specific humidity  $q$  over the 40 m vertical grid spacing, calculated between 400 and 1000 m altitude. (a),(c) 1600 UTC 2 Feb 2020 in a  $200 \text{ km} \times 100 \text{ km}$  domain simulation of trade wind cloudiness (“flower” pattern) in Dauhut et al. (2023); (b),(d) 1400 UTC, wherein the flower cloud is advected from right to left over the course of the simulation.

cloudiness. Because the cloud-free areas we observed are smaller than the circle scale (George et al. 2021), some signal is lost through this aggregation, but this approach enables a comparison to the mesoscale vertical velocity estimates. The strongest relationship,  $r = 0.40$ , is found between the *thickness* of the transition layer and cloud fraction at the level of its cloud-base maximum, whereas the correlation between the transition-layer *gradients* and cloud fraction ( $r = -0.31$ ) is weaker and of opposite sign, as would be expected if clouds were responsible for thickening the transition layer and weakening its gradients. The strength of the subsidence also shows a weak correlation with the strength of transition-layer gradients, with its magnitude ( $r = -0.34$ ) maximizing with subsidence estimated at a height of 1900 m, examining subsidence at levels between 400 and 4000 m at 10 m intervals. No meaningful relationship was found with any properties of the mixed layer.

From the conditional sampling, and the statistical analysis, a physical picture emerges that the life cycle of shallow clouds forming and dissipating in the transition layer changes vertical gradients relative to cloud-free conditions. The proposed physical mechanism—when shallow clouds dissipate or detrain about 100–200 m above the level where they form, they cool and moisten the environment, such that the ambient air more closely resembles the mixed-layer properties—is consistent with the observed differences in transition-layer structures in Fig. 8. And while the presence or absence of cloudiness may itself also depend on the strength of the shallow mesoscale overturning circulations (George et al. 2023), we assert that it is the strength of this cloud dissipation–driven mixing, which determines the strength of the transition-layer jumps.

#### d. Further support from large-eddy simulations

As a point of comparison, Fig. 9 shows that the large-eddy simulation output from Dauhut et al. (2023) exhibit a similar transition-layer structure, with stronger vertical gradients in large clear-sky areas than in areas influenced by clouds. For the simulations, we look at vertical differences from 400 to 1000 m, instead of 300 to 800 m in the dropsonde profiles because the mixed layer is deeper in the simulation; yet the results are qualitatively similar for different vertical ranges. The simulation vertical grid spacing is 40 m versus 10 m in the soundings; hence, there are larger jumps in Fig. 9 than for the soundings. These simulations further support that smoother vertical gradients in cloudy areas are not spurious observational error (e.g., slower sensor response times if a sonde became wet after passing through clouds; cf. Albright et al. 2022) and represent a physical difference that we endeavor to explain. Repeating a similar correlation analysis in the LES yields a consistent picture with, notably, a weak correlation between the strength of vertical velocity (coarsened to 5 km horizontal resolution to minimize the signal of updrafts and downdrafts and examined between 400 and 4000 m at 40 m vertical intervals) and the strength of the transition-layer gradient.

### 5. Implications of a cloudy transition layer

Clouds appear to be responsible for the observed transition-layer structure and its deviation from the canonical structure of a sharp jump in a dry convective boundary layer. It is less clear to what extent the emergence of a cloudy transition layer matters for the evolution of the mixed layer and, hence,



the net air–sea exchange of energy and moisture. Using “mixing diagrams” (Paluch 1979) and mixed-layer theory, we compare the structure of the lower atmosphere in (section 4) cloud-free (CFBL) and cloud-topped (CTBL) boundary layers. In both cases, however, the sondes are believed to sample primarily clear air. This comparison allows us to quantify the efficiency of mixing in the two cases, and the extent to which differences in the transition-layer structure imprint themselves on the mixed-layer properties.

*Mixing diagrams and mixed-layer theory*

To answer these questions, we apply mixed-layer theory to mixing diagrams. To introduce the ideas, we first examine the campaign-mean HALO dropsonde sounding through the lower 3 km. Figure 10 presents the mixing diagram of this sounding using potential temperature  $\theta$  and specific humidity  $q$  as thermodynamic coordinates. Each point in this space represents the mean across all 810 dropsondes at a given height. We use  $\theta$  and  $q$  coordinates because we almost exclusively sample clear skies, and they are ostensibly independent, at least insofar as any variables in a tightly coupled system are independent. Clearly the ability to follow additional tracers, such as ozone and dimethyl sulfide (e.g., Stevens et al. 2003), would augment our analysis, but such measurements were not made. Frameworks, based on moist conserved variables, such as the saturation point coordinate system of Betts (1982), might also be informative, but their interpretation is more nuanced and complicated by an inability to sample, or our lack of samples, of saturated air using the dropsondes.

A mixed layer shows up as a cluster of points around a single value, which in the case of Fig. 10 is around  $q = 15.4 \text{ g kg}^{-1}$  and  $\theta = 298.3 \text{ K}$ . Adiabatic mixing between layers of the atmosphere with distinct thermodynamic properties will scatter along a line spanning the space between the points that characterize the respective layers (e.g., Paluch 1979; Betts 1982; Betts and Albrecht 1987; Heus et al. 2008; Böing et al. 2014). Figure 10 shows that the same mixing line includes both the mixed and transition layers. This structure suggests that air in the transition layer is entrained into the mixed layer. The observed mixing line only changes its slope around 900 m, above the top of the subcloud layer, suggesting that air above this height is no longer directly incorporated into the mixed layer. For reference, Fig. 10 also plots the fundamental lines defined by constant- $\theta_v$  and constant- $\theta_e$  lines. This visualization shows that the subcloud layer, whose points are roughly aligned with a line of constant  $\theta_v$ , are better mixed in this quantity than in terms of either  $q$  or  $\theta$ . The constant- $\theta_e$  line shows the slope that a saturated, cloudy updraft would follow. The mixing line in the cloud layer more closely approaches a constant- $\theta_e$  line, suggesting that these two fundamental lines could be taken as limiting distributions for the subcloud versus the cloud layers.

A generalized budget equation for the value of a scalar,  $\bar{\vartheta}$  within the mixed layer, is derived in the appendix and can be expressed as

$$\bar{\vartheta} = \frac{\vartheta'_0 + A^* \vartheta_1}{(1 + A^*)} \quad \text{with} \quad \vartheta'_0 = \vartheta_0 + S_\vartheta \frac{h}{V_0}. \quad (2)$$

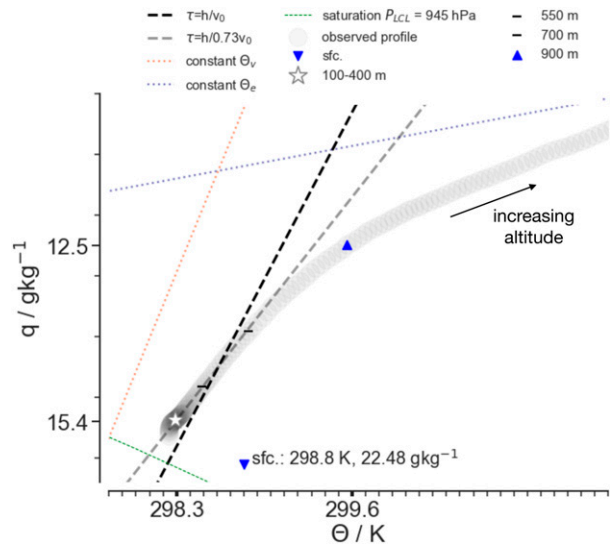


FIG. 10. Scatterplot of observed  $q$  and  $\theta$  values up to 3 km (gray points) and theoretical mixing lines from the surface to 3 km (black and gray dashed lines). Also shown are the campaign-mean surface value (blue downward triangle), values averaged from 100 to 400 m (white star), values at 550 and 700 m (approximate transition-layer extent), value at 900 m (blue upward triangle), constant lifting condensation level at 945 hPa (green dotted line), constant- $\theta_v$  line (orange dotted line), and constant- $\theta_e$  line (dark blue dotted line). Theoretical mixing lines are calculated from Eq. (2), as described in section 5. The black dashed line is the theoretical mixing line incorporating air from 10 to 150 m above the mixed layer. The gray dashed line multiplies the surface wind speed by 0.73.

This represents two point mixing between air above the boundary layer, whose properties are given by  $\vartheta_1$ , and surface values (denoted by  $\vartheta_0$ ) as modified by nonturbulent processes, i.e., advection, storage, or radiative heating. The strength of these nonturbulent processes are measured by  $S_\vartheta$  and act on a time scale  $\tau = h/V_0$ , with  $h$  the mixed-layer depth and  $V_0$  the surface exchange velocity (drag coefficient-weighted 10 m wind speed, see the appendix), which helps parameterize the surface turbulent fluxes. Equation (2) introduces an important quantity,  $A^*$ , a nondimensional entrainment rate, which defines the nondimensional entrainment velocity  $E = A^* V_0$ . It weights the influence of the surface (and nonturbulent processes) and the properties of the air being incorporated into the mixed layer on the state of the mixed layer.

We use Eq. (2) to calculate theoretical mixing lines whose slopes depend on the choices of  $q_1$  and  $\theta_1$  and whose end points are given by  $\vartheta'_0$ , varying  $A^*$ . To calculate  $\vartheta'_0$  we used the observed  $\vartheta_0$ ,  $Q_\vartheta$ , and  $h/V_0$  values from the soundings. We then find that the best-fit mixing line to the observations incorporates air from 10 to 150 m above the mixed-layer top (Fig. 10). The best fit mixing line diverges once the source region begins to extend above the transition layer and suggests that the transition layer is part of the same mixing layer as the mixed layer, and that the mixed-layer properties can be conceptualized as two point mixing between air at the top of the transition layer and air imbued with surface properties



modified by nonturbulent processes, as measured by  $Q_{\vartheta}$  acting on the time scale given by  $\tau = h/V_0$ .

The agreement of this theoretical mixing line, incorporating air from within the transition layer, with the observed values can be empirically improved by increasing  $\tau = h/V_0$ , for instance, by multiplying the wind speed by a factor 0.73 in the  $V_0$  term (Fig. 10, gray dashed line). These adjustments suggest potential limitations in how the surface exchange velocity is represented, or the effects of missing source terms, such as cloud induced perturbations to the radiative heating. Figure 10a also plots  $q$ - $\theta$  values corresponding to a constant lifting condensation level at 945 hPa. The observed and best-fit theoretical mixing line are nearly perpendicular to the constant lifting condensation level curve. Whether this is a coincidence, or whether mixing aligns to maximize variance in the lifting condensation level, merits further study, and perhaps would benefit from an analysis using moist-conservative coordinates as in Betts (1982).

### 1) EFFECT OF A CLOUDY TRANSITION LAYER ON ENTRAINMENT

Given the mixing line connecting  $\vartheta'_0$  with  $\vartheta_1$ , the nondimensional entrainment rate  $A^*$  can be measured by inverting Eq. (2). By deriving  $A^*$  from soundings taken in regions without clouds, versus soundings from regions with scattered clouds (albeit the soundings are still assumed to have fallen through some clear skies), it should be possible to identify if the presence of a cloud-maintained transition layer leads to changes in the rate of sub-cloud-layer deepening, i.e., greater values of  $A^*$ .

The resulting mixing diagrams are shown in Fig. 11. Both seem to show that the cluster of mixed-layer points lie at about the same distance along the mixing line, suggesting at least that differences in  $A^*$  are subtle. More quantitatively, given  $\{\vartheta'_0, \bar{\vartheta}, \vartheta_1\}$ , Eq. (2) can be inverted for  $A^*$ . We follow this procedure for each case, estimating  $\vartheta'_0$  by assuming both cases have the same  $\vartheta_0$ , but allowing  $Q_{\vartheta}$  to vary (giving  $\theta'_0 = 297.1$  K and  $q'_0 = 21.1$  g kg $^{-1}$  for the CFBL and  $\theta'_0 = 297.1$  K and  $q'_0 = 21.4$  g kg $^{-1}$  for the CTBL profile). In this case,  $\vartheta_1$  is chosen as the point where a data-derived mixing line (a linear regression to observations from 400 to 700 m) departs from the observations by 0.1 g kg $^{-1}$ , a point whose location and height are included on the diagram. This analysis suggests that  $A^*$  is slightly smaller (3.1) in the CFBL as compared to the CTBL (3.3) case. This result is consistent with the notion that the life cycle of shallow clouds grows the transition-layer structure. As a consistency check we apply the same procedure for  $\theta$  to estimate  $A^*$ , it also yields a larger  $A^*$  value for cloudy than large cloud-free area profiles.

The differences in  $A^*$  are, however, small and equivocal. That our analysis does not identify a substantial change in  $A^*$  between boundary layers largely devoid of clouds, versus those in which clouds are present, suggests that the clouds are not a first-order influence on the rate of mixing. The main difference appears to be that the clouds modify the properties of the air that is being incorporated into the mixed layer, rather than the rate at which it is being incorporated, as we discuss in the next section.

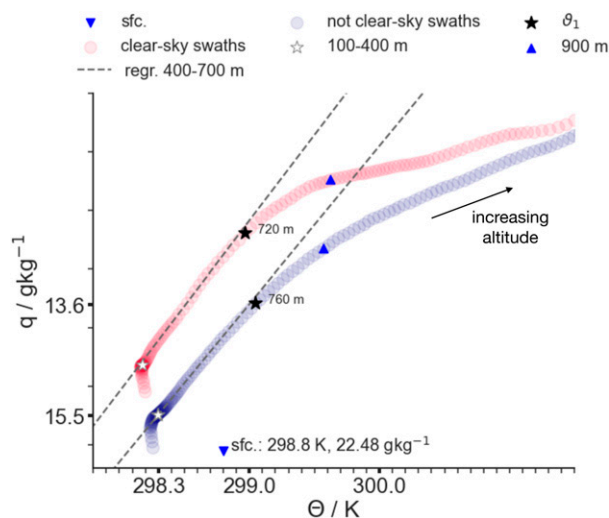


FIG. 11. As in Fig. 10, but for  $q$  and  $\theta$  soundings aggregated for large clear-sky areas (red) and areas influenced by cloudiness (blue, following the conditional sampling in Fig. 6). Also shown are the campaign-mean surface value (blue downward triangles), value averaged from 100 to 400 m (white stars),  $\vartheta_1$  value annotated with its height (black stars), and value at 900 m (blue upward triangles). Data-derived mixing lines are linear regressions to the observed profile from 400 to 700 m (gray dotted lines).

### 2) EFFECT OF A CLOUDY TRANSITION LAYER ON THE MIXED LAYER

That the differences in the transition-layer state influence the mixed layer and hence surface fluxes is apparent in Fig. 11. The mixing line of the cloud-free soundings is clearly distinct from that of the cloudy soundings, mostly by virtue of the value of  $\vartheta_1$ .

Were this not the case we would expect the value of  $\vartheta_1$  to lie on the mixing line of the CTBL soundings, albeit extending to a drier and warmer state. That this is not the case can mostly be attributed to differences in  $q_1$ , suggesting that the main role of the clouds is to moisten the transition layer, rather than to cool it—noting that this moistening arises because much of the condensate reevaporates, rather precipitates.

To illustrate this idea, we consider a case of a “dry transition layer.” That is, instead of incorporating the campaign-mean transition-layer air (averaged between 550 and 700 m), we incorporate air from higher aloft that is assumed to subside without evaporative cooling of cloud liquid water. This case would imply a stronger jump in the transition layer. To estimate such an example  $q_1$ - $\theta_1$  pair, we consider the campaign-mean specific humidity at 1500 m (having a value of 10.03 g kg $^{-1}$ ) and find the corresponding  $\theta$  value such that the  $\theta_v$  value at 1500 m equals its mean transition-layer value. A constant  $\theta_v$  is motivated by the idea that gravity waves will remove buoyancy differences at similar levels, e.g., between the observed transition-layer value and our “dry transition layer” example. Adopting  $q_1$  and  $\theta_1$  values of 10.03 g kg $^{-1}$  and 299.4 K as  $\vartheta_1$  values and predicting the mixed-layer  $q$ - $\theta$  pair following Eq. (2) yields a predicted mixed-layer mean value of 298.9 K and 11.8 g kg $^{-1}$ . We set  $A^* = 5$  and otherwise keep terms equal to the values in the adjusted mixing line (gray dashed line in

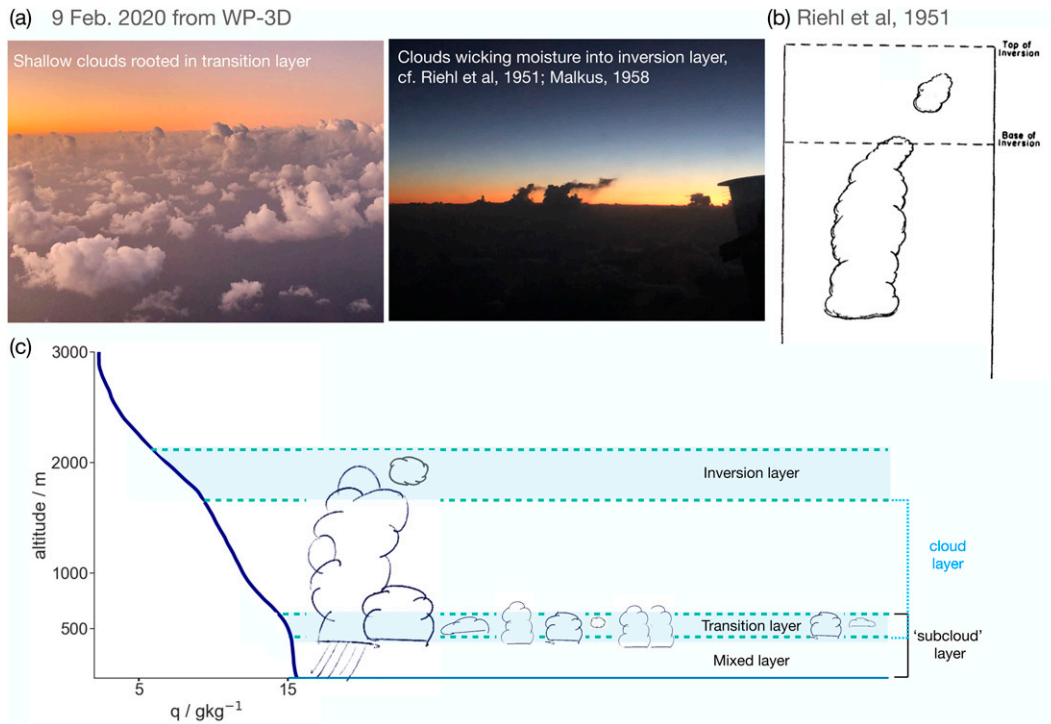


FIG. 12. (a) Photos taken during a EUREC<sup>4</sup>A flight in the WP-3D aircraft that illustrate the ubiquity of very shallow clouds, (left) often with their bases in the transition layer and (right) deeper clouds wicking or injecting moisture to maintain the inversion layer as in the mechanism proposed by Riehl et al. (1951). (b) Reproducing a schematic from Riehl et al. (1951), who proposed that the evaporation of deeper clouds maintains the trade wind inversion layer. (c) Illustration of a conceptual picture suggesting a symmetry between deeper clouds growing and maintaining the trade wind inversion layer following Riehl et al. (1951) and Stevens (2007), and shallower clouds growing the transition layer. The dissipation of shallow clouds in the transition layer moistens and cools (denoted by the transparent blue area) the transition layer, rendering gradients smoother and weaker compared to the dry boundary layer case.

Fig. 10). These values are warmer and drier than the prediction using  $\theta_1$ - $q_1$  values in the transition layer, which were 298.3 K and 15.44  $\text{g kg}^{-1}$ . This comparison suggests that the presence of a cloudy transition layer leads to a moister and cooler mixed layer compared to that of a cloud-free transition layer (noting that entrainment still dries and warms the layer in absolute terms). These differences largely compensate in terms of buoyancy, and thus have a negligible influence on the energetics.

**6. Conclusions**

In the trades, we observe a transition-layer structure with a finite thickness (about 150 m) and smooth vertical gradients compared to a jump. We identify the transition layer from thermodynamic soundings, as a region above the mixed layer, within which the specific humidity gradients approximately balance the potential temperature gradients to maintain a layer of nearly constant virtual potential temperature. This layer is almost always extended; jumps, or sharp changes in conserved quantities at the top of the mixed layer—as, for instance, are familiar from studies of stratocumulus and to a lesser degree over clear convective boundary layers—are rare, and tend to occur in scenes that are cloud-free over large [ $O(200)$  km] areas. In areas where

clouds are actively ventilating the mixed layer, and which also extend to momentarily unsaturated areas between the clouds, the transition of the thermodynamic profiles of potential temperature and specific humidity to their free-tropospheric values are more gradual. Analysis of ceilometer and lidar data from several sites finds evidence for two populations of clouds: shallow clouds with bases near the top of the mixed layer and a vertical depth commensurate with the depth of the transition layer, and a population of deep clouds that extend through the about 1500-m-deep cloud layer. The second population, of deeper clouds, is always accompanied by the first, but not vice versa. This allows us to establish that the presence of shallow clouds is sufficient to maintain the transition-layer structure as it is found irrespective of whether deep clouds are present or not.

Based on these findings, we propose a conceptual picture whereby the transition layer is maintained by the formation and dissipation of shallow clouds. That is, the transition-layer structure is predominantly determined by cloudy, not dry processes—although dry processes, like enhanced subsidence from nearby regions of more active convection may lead to the absence of clouds. We argue that the transition layer is maintained by a population of shallow clouds analogously to the way a population of deeper clouds maintains the trade

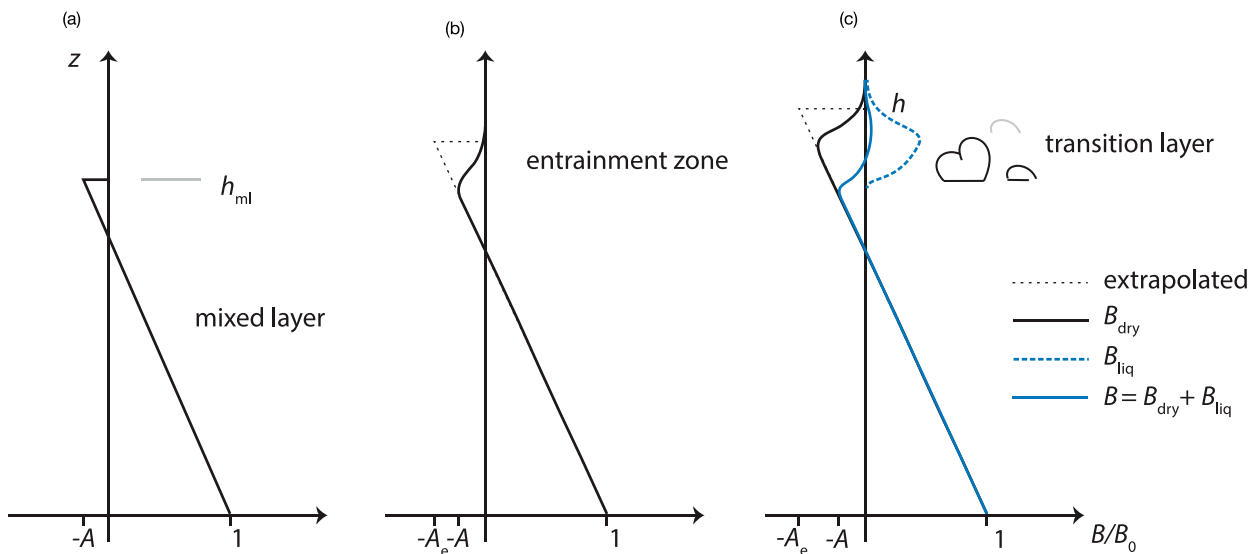


FIG. 13. Profiles of the ratio of the buoyancy flux to its surface buoyancy flux for different cases, which are used to illustrate the entrainment efficiency  $A$  or its effective value  $A_e$ . (a) The classical mixed-layer model view of an abrupt discontinuity at the mixed-layer top, wherein  $A$  is the minimum ratio of the buoyancy flux to its surface value and is found at the layer top. (b) This view is contrasted with a finite-thickness transition layer in which the minimum buoyancy flux (corresponding to  $A$ ) is not found at the mixed-layer top, but rather  $A_e$  extrapolated (in the dotted black line) to the layer top is the value required to obtain the correct mixed-layer heating and cooling rates from the slope of the buoyancy profile. (c) Illustration of how the liquid water flux (dotted blue line) can contribute to the net buoyancy flux (solid blue line) and compensate for more negative (extrapolated, dotted black line) dry buoyancy fluxes and larger  $A_e$ . The contribution of the liquid water flux can be thought of as an additional “boost” to the energetics of entrainment mixing.

wind inversion. The mechanism is qualitatively explained by Riehl et al. (1951) who write,

It is well known that the bases of the cumuli have a nearly uniform height, but that the tops are very irregular. Some are found within the cloud layer, many near the inversion base, and some within the inversion layer as active clouds penetrate the base. As shown by visual observation and many photographs, the tops of these clouds break off and evaporate quickly. In this way moisture is introduced into the lower portions of the inversion layer, and the air there situated gradually takes on the characteristics of the cloud layer.

and described quantitatively by Stevens (2007) These ideas are further illustrated with the help of Fig. 12b, which we adapt from Riehl et al. (1951). In a similar way, we propose that a population of shallow clouds, forming at the top of the mixed layer and evaporating in the lower part of the cloud layer, thicken the layer over which the thermodynamic profiles transition between their mixed-layer and cloud-layer values. As such, within cloud-topped boundary layers, the transition layer forms analogously to the trade wind inversion layer, albeit through the action of shallower clouds (Fig. 12c). By moistening and destabilizing the lower cloud layer small clouds “precondition” the large-scale environment and decrease the resistance to convection by weakening vertical gradients in the transition layer, making the lower cloud layer less hostile to the development of deeper convection. This process suggests that smaller clouds beget larger clouds, in ways reminiscent of the “acceleration-detrainment layer” proposed by Neggers (2015).

Shallow clouds support the development of a deeper *mixing* layer, albeit not a deeper *mixed* layer. Stevens (2007) showed

that the additional work required to maintain the quasi equilibrium of such an extended mixing layer, can be provided by the linearly increasing liquid water flux within the cloud layer. We simply extend these ideas to the case of mixing dominated by a shallow population of clouds, who maintain the transition layer in this fashion. The basic idea is presented with the help of Fig. 13. This schematic distinguishes between the minimum of the nondimensional buoyancy flux  $A$  from its effective value  $A_e$ , obtained by extending the region of linear fluxes to the top of the mixing layer, as would be required to maintain the same rate of warming and drying over a mixed layer as deep as the mixing layer. The value of  $A_e$  is thereby larger than the canonical value of  $A \approx 0.2$  and rationalizes the finding of Albright et al. (2022) wherein an entrainment formulation based on mixed-layer theory and dry boundary layers was used, but required a much larger value of  $A$  to reproduce the observed mixed-layer heat and moisture balances.

Although clouds influence the value of  $A_e$ , we find no evidence that they strongly influence the rate of mixing, as measured by the entrainment velocity. Comparing mixing diagrams in large cloud-free regions, and regions where a transition layer is maintained by fields of shallow transition-layer clouds, at most a small (10%), but not significant, increase in the mixing can be identified. This implies that the larger values of  $A_e$  needed to explain the mixed-layer heat and moisture balances, as in Albright et al. (2022), are mostly balanced by proportionally larger effective jumps in the buoyancy at the top of the mixed layer. The main effect of shallow transition-layer clouds thus appears to be to precondition a shallow layer in ways that modify the

development of the mixed layer and make it easier for deeper trade wind clouds to develop and organize. To the extent that areas of deeper and more organized trade wind convection enhance subsidence in their environment and thereby suppress shallow clouds, it suggests that the development and organization of clouds in the trades might depend on the interplay between these two populations of clouds, with shallow clouds sheltering the boundary layer and deeper clouds ventilating it.

*Acknowledgments.* A.L.A., S.B., and R.V. gratefully acknowledge support from the European Research Council (ERC) under the European Union’s Horizon 2020 research and innovation programme (EUREC<sup>4</sup>A Grant Agreement 694768). We thank Thibaut Dauhut for providing data from his large-eddy simulations. We would also like to thank Martin Janssens, Franziska Glassmeier, and Pier Siebesma for helpful discussions at the TU Delft as we were revising this manuscript. We are grateful to Alan Betts and Paquita Zuidema for their insightful comments during the revision process that greatly strengthened our manuscript, and Elie Bou-Zeid for serving as editor.

*Data availability statement.* JOANNE data are available at <https://doi.org/10.25326/246>. All EUREC<sup>4</sup>A data are also accessible at <https://observations.ipsl.fr/aeris/eurec4a-data/>. For instance, WALES cloud-top height data are accessible at <https://observations.ipsl.fr/aeris/eurec4a-data/AIRCRAFT/HALO/WALES-LIDAR/cloudtop/>, and BCO ceilometer cloud-base height data are at <https://observations.ipsl.fr/aeris/eurec4a-data/BARBADOS/BCO/Ceilometer/nfiles/>. Large-eddy simulation data from Dauhut et al. (2023) can be found at <https://observations.ipsl.fr/aeris/eurec4a-data/SIMULATIONS/LES-02FEB20-MesoNH-v0-1/>.

APPENDIX

**Derivation for Theoretical Mixing Line Equation from Mixed-Layer Theory**

As discussed in Stevens (2006), for a mixed-layer scalar  $\vartheta$  after performing a Reynolds decomposition on the conservation equation ( $D\vartheta/Dt = Q_\vartheta$ , where  $Q_\vartheta$  is a diabatic source term) and integrating over the depth of the layer, the mixed-layer budget of  $\vartheta$  can be written as

$$hS_\vartheta = \overline{w'\vartheta'}|_0 - \overline{w'\vartheta'}|_1, \tag{A1}$$

We neglect the horizontal gradients in  $\overline{w'\vartheta'}$ , which are small compared to the vertical gradients.  $S_\vartheta$  includes the contribution of the mean flow to the material derivative (including the storage term and horizontal advection), as well as the diabatic source term  $Q_\vartheta$ . This diabatic source term  $Q_\vartheta$  can include radiation or precipitation and evaporation effects. We set  $Q_q = 0$  for moisture, neglecting the influence of evaporating precipitation on the subcloud-layer moisture budget, but we do account for radiation in the heat budget using clear-sky, aerosol-free radiative heating

profiles ( $Q_\theta \neq 0$ ). The equation expresses that the vertical divergence of the turbulent flux balances the  $S_\vartheta$  term, times the thickness of the layer,  $h$  (e.g., Betts 1976; Stevens 2006). Note that here,  $h$  refers to the mixed-layer top given our focus on processes in the transition layer above the mixed-layer top. The subscript 0 denotes values at the lower interface of the bulk layer (ocean-to-mixed-layer interface), and the subscript 1 denotes values at the upper interface (the mixed-layer-to-transition-layer interface), and  $w$  refers to the vertical velocity.

Two closure assumptions are commonly used regarding Eq. (A1). First, the flux at an interface  $i$  is expressed as the product of the velocity relative to the mean flow and a “jump,”

$$\overline{w'\vartheta'}|_i = -V_i\Delta_i\vartheta, \tag{A2}$$

where  $\Delta_i\vartheta$  defines the change in  $\vartheta$  across the interface, from top to bottom, so that  $\Delta_1\vartheta = \vartheta_1 - \vartheta$  and  $\Delta_0\vartheta = \vartheta - \vartheta_0$ .

With this notation, we can rewrite Eq. (A1) as

$$hS_\vartheta = -V_0\Delta_0\vartheta + V_1\Delta_1\vartheta. \tag{A3}$$

Second, it is assumed that the  $\theta_v$  flux (proportional to the buoyancy flux) at the upper interface is energetically constrained by its source of surface  $\theta_v$  fluxes, such that

$$V_1\Delta_1\theta_v = -A_eV_0\Delta_0\theta_v, \tag{A4}$$

with  $A_e$  defining the entrainment efficiency and assumed to be constant. In Albright et al. (2022), a mean value  $A_e = 0.43$  was found from a Bayesian inversion of uncertain entrainment parameters in subcloud-layer thermodynamic budgets closed with EUREC<sup>4</sup>A data.

With this second closure assumption in Eq. (A4) and taking  $\vartheta = \theta_v$ , Eq. (A3) becomes

$$-V_0(1 + A_e)\Delta_0\theta_v = hS_{\theta_v}. \tag{A5}$$

Rearranging Eq. (A5) to solve for the  $\theta_v$  jump at the surface yields

$$\Delta_0\theta_v = -\frac{hS_{\theta_v}}{V_0(1 + A_e)}. \tag{A6}$$

With Eq. (A6), Eq. (A4) can be manipulated to solve for the velocity at the upper interface,  $V_1$ :

$$V_1 = A^*V_0 \quad \text{where} \quad A^* = -\frac{\Delta_0\theta_v}{\Delta_1\theta_v}. \tag{A7}$$

The modified constant  $A^*$  is similar to the effective entrainment buoyancy flux ratio  $A_e$ ; whereas  $A_e$  relates the buoyancy flux at the upper and lower interfaces,  $A^*$  is a nondimensional parameter relating the surface exchange buoyancy jump to the jump at the upper interface.  $A^*$  is, however, not energetically constrained by the surface buoyancy source (e.g., that the buoyancy flux used at the upper interface is generated at the surface, such that  $A_e$  cannot exceed one).



Using the above formulations, including  $A^*$ , the generalized budget equation in Eq. (A3) can be solved for  $\bar{\vartheta}$ :

$$\bar{\vartheta} = \frac{\vartheta_0 + A^* \vartheta_1 + S_g \tau}{(1 + A^*)}, \quad \text{where} \quad \tau = \frac{h}{V_0}. \quad (\text{A8})$$

## REFERENCES

- Albrecht, B. A., A. K. Betts, W. H. Schubert, and S. K. Cox, 1979: Model of the thermodynamic structure of the trade-wind boundary layer: Part I. Theoretical formulation and sensitivity tests. *J. Atmos. Sci.*, **36**, 73–89, [https://doi.org/10.1175/1520-0469\(1979\)036<0073:MOTTSO>2.0.CO;2](https://doi.org/10.1175/1520-0469(1979)036<0073:MOTTSO>2.0.CO;2).
- Albright, A. L., B. Fildier, L. Touzé-Peiffer, R. Pincus, J. Vial, and C. Muller, 2021: Atmospheric radiative profiles during EUREC<sup>4</sup>A. *Earth Syst. Sci. Data*, **13**, 617–630, <https://doi.org/10.5194/essd-13-617-2021>.
- , S. Bony, B. Stevens, and R. Vogel, 2022: Observed subcloud layer moisture and heat budgets in the trades. *J. Atmos. Sci.*, **79**, 2363–2385, <https://doi.org/10.1175/JAS-D-21-0337.1>.
- Arakawa, A., and W. H. Schubert, 1974: Interaction of a cumulus cloud ensemble with the large-scale environment, part I. *J. Atmos. Sci.*, **31**, 674–701, [https://doi.org/10.1175/1520-0469\(1974\)031<0674:IOACCE>2.0.CO;2](https://doi.org/10.1175/1520-0469(1974)031<0674:IOACCE>2.0.CO;2).
- Augstein, E., H. Schmidt, and F. Ostapoff, 1974: The vertical structure of the atmospheric planetary boundary layer in undisturbed trade winds over the Atlantic Ocean. *Bound.-Layer Meteor.*, **6**, 129–150, <https://doi.org/10.1007/BF00232480>.
- Betts, A. K., 1976: Modeling subcloud layer structure and interaction with shallow cumulus layer. *J. Atmos. Sci.*, **33**, 2363–2382, [https://doi.org/10.1175/1520-0469\(1976\)033<2363:MSLSAI>2.0.CO;2](https://doi.org/10.1175/1520-0469(1976)033<2363:MSLSAI>2.0.CO;2).
- , 1982: Saturation point analysis of moist convective overturning. *J. Atmos. Sci.*, **39**, 1484–1505, [https://doi.org/10.1175/1520-0469\(1982\)039<1484:SPAOMC>2.0.CO;2](https://doi.org/10.1175/1520-0469(1982)039<1484:SPAOMC>2.0.CO;2).
- , and B. A. Albrecht, 1987: Conserved variable analysis of the convective boundary layer thermodynamic structure over the tropical oceans. *J. Atmos. Sci.*, **44**, 83–99, [https://doi.org/10.1175/1520-0469\(1987\)044<0083:CVAOTC>2.0.CO;2](https://doi.org/10.1175/1520-0469(1987)044<0083:CVAOTC>2.0.CO;2).
- Böing, S. J., H. J. J. Jonker, W. A. Nawara, and A. P. Siebesma, 2014: On the deceiving aspects of mixing diagrams of deep cumulus convection. *J. Atmos. Sci.*, **71**, 56–68, <https://doi.org/10.1175/JAS-D-13-0127.1>.
- Bony, S., and B. Stevens, 2019: Measuring area-averaged vertical motions with dropsondes. *J. Atmos. Sci.*, **76**, 767–783, <https://doi.org/10.1175/JAS-D-18-0141.1>.
- , and Coauthors, 2017: EUREC<sup>4</sup>A: A field campaign to elucidate the couplings between clouds, convection and circulation. *Surv. Geophys.*, **38**, 1529–1568, <https://doi.org/10.1007/s10712-017-9428-0>.
- , H. Schulz, J. Vial, and B. Stevens, 2020: Sugar, gravel, fish, and flowers: Dependence of mesoscale patterns of trade-wind clouds on environmental conditions. *Geophys. Res. Lett.*, **47**, e2019GL085988, <https://doi.org/10.1029/2019GL085988>.
- , and Coauthors, 2022: EUREC<sup>4</sup>A observations from the SAFIRE ATR42 aircraft. *Earth Syst. Sci. Data*, **14**, 2021–2064, <https://doi.org/10.5194/essd-14-2021-2022>.
- Canut, G., F. Couvreur, M. Lothon, D. Pino, and F. Saïd, 2012: Observations and large-eddy simulations of entrainment in the sheared Sahelian boundary layer. *Bound.-Layer Meteor.*, **142**, 79–101, <https://doi.org/10.1007/s10546-011-9661-x>.
- Dauhut, T., and Coauthors, 2023: Flower trade-wind clouds are shallow mesoscale convective systems. *Quart. J. Roy. Meteor. Soc.*, **149**, 325–347, <https://doi.org/10.1002/qj.4409>.
- Garcia, J. R., and J. P. Mellado, 2014: The two-layer structure of the entrainment zone in the convective boundary layer. *J. Atmos. Sci.*, **71**, 1935–1955, <https://doi.org/10.1175/JAS-D-13-0148.1>.
- Genkova, I., G. Seiz, P. Zuidema, G. Zhao, and L. Di Girolamo, 2007: Cloud top height comparisons from ASTER, MISR, and MODIS for trade wind cumuli. *Remote Sens. Environ.*, **107**, 211–222, <https://doi.org/10.1016/j.rse.2006.07.021>.
- Gentine, P., A. K. Betts, B. R. Lintner, K. L. Findell, C. C. van Heerwaarden, and F. D’Andrea, 2013: A probabilistic bulk model of coupled mixed layer and convection. Part II: Shallow convection case. *J. Atmos. Sci.*, **70**, 1557–1576, <https://doi.org/10.1175/JAS-D-12-0146.1>.
- George, G., and Coauthors, 2021: JOANNE: Joint dropsonde Observations of the Atmosphere in tropical North Atlantic meso-scale Environments. *Earth Syst. Sci. Data*, **13**, 5253–5272, <https://doi.org/10.5194/essd-13-5253-2021>.
- , B. Stevens, S. Bony, R. Vogel, and A. K. Naumann, 2023: Ubiquity of shallow mesoscale circulations in the trades and their influence on moisture variance. *Nat. Geosci.*, in press.
- Heus, T., G. van Dijk, H. J. J. Jonker, and H. E. A. Van den Akker, 2008: Mixing in shallow cumulus clouds studied by Lagrangian particle tracking. *J. Atmos. Sci.*, **65**, 2581–2597, <https://doi.org/10.1175/2008JAS2572.1>.
- Jacob, M., P. Kollias, F. Ament, V. Schemann, and S. Crewell, 2020: Multilayer cloud conditions in trade wind shallow cumulus—Confronting two ICON model derivatives with airborne observations. *Geosci. Model Dev.*, **13**, 5757–5777, <https://doi.org/10.5194/gmd-13-5757-2020>.
- Konow, H., and Coauthors, 2021: EUREC<sup>4</sup>A’s HALO. *Earth Syst. Sci. Data*, **13**, 5545–5563, <https://doi.org/10.5194/essd-13-5545-2021>.
- Leahy, L. V., R. Wood, R. J. Charlson, C. A. Hostetler, R. R. Rogers, M. A. Vaughan, and D. M. Winker, 2012: On the nature and extent of optically thin marine low clouds. *J. Geophys. Res.*, **117**, D22201, <https://doi.org/10.1029/2012JD017929>.
- Lilly, D. K., 1968: Models of cloud-topped mixed layers under a strong inversion. *Quart. J. Roy. Meteor. Soc.*, **94**, 292–309, <https://doi.org/10.1002/qj.49709440106>.
- Lonitz, K., B. Stevens, L. Nuijens, V. Sant, L. Hirsch, and A. Seifert, 2015: The signature of aerosols and meteorology in long-term cloud radar observations of trade wind cumuli. *J. Atmos. Sci.*, **72**, 4643–4659, <https://doi.org/10.1175/JAS-D-14-0348.1>.
- Malkus, J. S., 1958: On the structure of the trade wind moist layer. MIT and WHOI Papers in Physical Oceanography and Meteorology, Vol. 13, No. 2, 47 pp., <https://darchive.mblwhoilibrary.org/bitstream/handle/1912/1065/Vol.%2013%20No.%202.pdf?sequence=1&isAllowed=y>.
- Mieslinger, T., Á. Horváth, S. A. Buehler, and M. Sakradzija, 2019: The dependence of shallow cumulus macrophysical properties on large-scale meteorology as observed in ASTER imagery. *J. Geophys. Res. Atmos.*, **124**, 11 477–11 505, <https://doi.org/10.1029/2019JD030768>.
- Neggers, R. A. J., 2015: Exploring bin-macrophysics models for moist convective transport and clouds. *J. Adv. Model. Earth Syst.*, **7**, 2079–2104, <https://doi.org/10.1002/2015MS000502>.
- , B. Stevens, and J. D. Neelin, 2006: A simple equilibrium model for shallow-cumulus-topped mixed layers. *Theor.*

- Comput. Fluid Dyn.*, **20**, 305–322, <https://doi.org/10.1007/s00162-006-0030-1>.
- , M. Köhler, and A. C. Beljaars, 2009: A dual mass flux framework for boundary layer convection. Part I: Transport. *J. Atmos. Sci.*, **66**, 1465–1487, <https://doi.org/10.1175/2008JAS2635.1>.
- Nicholls, S., and M. A. Lemone, 1980: The fair weather boundary layer in GATE: The relationship of subcloud fluxes and structure to the distribution and enhancement of cumulus clouds. *J. Atmos. Sci.*, **37**, 2051–2067, [https://doi.org/10.1175/1520-0469\(1980\)037<2051:TFWBLL>2.0.CO;2](https://doi.org/10.1175/1520-0469(1980)037<2051:TFWBLL>2.0.CO;2).
- Nuijens, L., I. Serikov, L. Hirsch, K. Lonitz, and B. Stevens, 2014: The distribution and variability of low-level cloud in the North Atlantic trades. *Quart. J. Roy. Meteor. Soc.*, **140**, 2364–2374, <https://doi.org/10.1002/qj.2307>.
- Ooyama, K., 1971: A theory on parameterization of cumulus convection. *J. Meteor. Soc. Japan*, **49**, 744–756, [https://doi.org/10.2151/jmsj1965.49A.0\\_744](https://doi.org/10.2151/jmsj1965.49A.0_744).
- Orlanski, I., 1975: A rational subdivision of scales for atmospheric processes. *Bull. Amer. Meteor. Soc.*, **56**, 527–530, <https://doi.org/10.1175/1520-0477-56.5.527>.
- Paluch, I. R., 1979: The entrainment mechanism in Colorado cumuli. *J. Atmos. Sci.*, **36**, 2467–2478, [https://doi.org/10.1175/1520-0469\(1979\)036<2467:TEMICC>2.0.CO;2](https://doi.org/10.1175/1520-0469(1979)036<2467:TEMICC>2.0.CO;2).
- Riehl, H., T. C. Yeh, J. S. Malkus, and N. E. la Seur, 1951: The north-east trade of the Pacific Ocean. *Quart. J. Roy. Meteor. Soc.*, **77**, 598–626, <https://doi.org/10.1002/qj.49707733405>.
- Stevens, B., 2006: Bulk boundary-layer concepts for simplified models of tropical dynamics. *Theor. Comput. Fluid Dyn.*, **20**, 279–304, <https://doi.org/10.1007/s00162-006-0032-z>.
- , 2007: On the growth of layers of nonprecipitating cumulus convection. *J. Atmos. Sci.*, **64**, 2916–2931, <https://doi.org/10.1175/JAS3983.1>.
- , and Coauthors, 2001: Simulations of trade wind cumuli under a strong inversion. *J. Atmos. Sci.*, **58**, 1870–1891, [https://doi.org/10.1175/1520-0469\(2001\)058<1870:SOTWCU>2.0.CO;2](https://doi.org/10.1175/1520-0469(2001)058<1870:SOTWCU>2.0.CO;2).
- , and Coauthors, 2003: Dynamics and Chemistry of Marine Stratocumulus—DYCOMS-II. *Bull. Amer. Meteor. Soc.*, **84**, 579–594, <https://doi.org/10.1175/BAMS-84-5-579>.
- , and Coauthors, 2016: The Barbados Cloud Observatory: Anchoring investigations of clouds and circulation on the edge of the ITCZ. *Bull. Amer. Meteor. Soc.*, **97**, 787–801, <https://doi.org/10.1175/BAMS-D-14-00247.1>.
- , and Coauthors, 2020: Sugar, gravel, fish and flowers: Mesoscale cloud patterns in the trade winds. *Quart. J. Roy. Meteor. Soc.*, **146**, 141–152, <https://doi.org/10.1002/qj.3662>.
- , and Coauthors, 2021: EUREC<sup>4</sup>A. *Earth Syst. Sci. Data*, **13**, 4067–4119, <https://doi.org/10.5194/essd-13-4067-2021>.
- Stull, R. B., 1976: The energetics of entrainment across a density interface. *J. Atmos. Sci.*, **33**, 1260–1267, [https://doi.org/10.1175/1520-0469\(1976\)033<1260:TEOEAD>2.0.CO;2](https://doi.org/10.1175/1520-0469(1976)033<1260:TEOEAD>2.0.CO;2).
- Tennekes, H., 1973: A model for the dynamics of the inversion above a convective boundary layer. *J. Atmos. Sci.*, **30**, 558–567, [https://doi.org/10.1175/1520-0469\(1973\)030<0558:AMFTDO>2.0.CO;2](https://doi.org/10.1175/1520-0469(1973)030<0558:AMFTDO>2.0.CO;2).
- Touzé-Peiffer, L., R. Vogel, and N. Rochetin, 2022: Cold pools observed during EUREC<sup>4</sup>A: Detection and characterization from atmospheric soundings. *J. Appl. Meteor. Climatol.*, **61**, 593–610, <https://doi.org/10.1175/JAMC-D-21-0048.1>.
- Vial, J., and Coauthors, 2019: A new look at the daily cycle of trade wind cumuli. *J. Adv. Model. Earth Syst.*, **11**, 3148–3166, <https://doi.org/10.1029/2019MS001746>.
- Vogel, R., A. L. Albright, J. Vial, G. George, B. Stevens, and S. Bony, 2022: Strong cloud–circulation coupling explains weak trade cumulus feedback. *Nature*, **612**, 696–700, <https://doi.org/10.1038/s41586-022-05364-y>.
- Wirth, M., A. Fix, P. Mahnke, H. Schwarzer, F. Schrandt, and G. Ehret, 2009: The airborne multi-wavelength water vapor differential absorption lidar WALES: System design and performance. *Appl. Phys.*, **96B**, 201–213, <https://doi.org/10.1007/s00340-009-3365-7>.
- Yin, B., and B. A. Albrecht, 2000: Spatial variability of atmospheric boundary layer structure over the eastern equatorial Pacific. *J. Climate*, **13**, 1574–1592, [https://doi.org/10.1175/1520-0442\(2000\)013<1574:SVOABL>2.0.CO;2](https://doi.org/10.1175/1520-0442(2000)013<1574:SVOABL>2.0.CO;2).